J. Fluid Mech. (1994), *vol.* 268, *pp.* 1–36

Crossflow disturbances in three-dimensional boundary layers: nonlinear development, wave interaction and secondary instability

By M. R. MALIK, F. LI AND C.-L. CHANG
High Technology Corporation, PO Box 7262, Hampton, VA 23666, USA

(Received 15 February 1993 and in revised form 16 October 1993)

Nonlinear stability of a model swept-wing boundary layer, subject to crossflow instability, is investigated by numerically solving the governing partial differential equations. The three-dimensional boundary layer is unstable to both stationary and travelling crossflow disturbances. Nonlinear calculations have been carried out for stationary vortices and the computed wall vorticity pattern results in streamwise streaks which resemble quite well the surface oil-flow visualizations in swept-wing experiments. Other features of the stationary vortex development (half-mushroom structure, inflected velocity profiles, vortex doubling, etc.) are also captured in these calculations. Nonlinear interaction of the stationary and travelling waves is also studied. When initial amplitude of the stationary vortex is larger than the travelling mode, the stationary vortex dominates most of the downstream development. When the two modes have the same initial amplitude, the travelling mode dominates the downstream development owing to its higher growth rate. It is also found that, prior to laminar/turbulent transition, the three-dimensional boundary layer is subject to a high-frequency secondary instability, which is in agreement with the experiments of Poll (1985) and Kohama, Saric & Hoos (1991). The frequency of this secondary instability, which resides on top of the stationary crossflow vortex, is an order of magnitude higher than the frequency of the most-amplified travelling crossflow mode.

1. Introduction

In swept-wing flows, a chordwise pressure gradient near the leading edge causes inviscid streamlines to be curved in the planes parallel to the wing surface. Associated with this streamline curvature is a pressure gradient which acts in a direction normal to the streamlines and introduces a secondary flow within the boundary layer. This secondary flow, commonly known as crossflow, is subject to inviscid instability due to the presence of an inflection point (Gregory, Stuart & Walker 1955) and is the main cause of transition in swept-wing flows. Thus, this problem is not only of fundamental importance in fluid mechanics but also of prime significance in laminar flow control design of swept wings.

Crossflow instability often results in the formation of stationary corotating vortices commonly called crossflow vortices. This phenomenon is observed in swept-wing boundary layers as well as in other geometries such as rotating disks and cones. How the stationary crossflow vortices lead to turbulence remains unknown. Travelling crossflow disturbances are also possible and the role of travelling *vs.* stationary disturbances is a question which needs to be investigated. Another problem which is of interest in swept-wing flows is the possibility of interaction between the inviscid

crossflow disturbances and viscous streamwise instability. Crossflow disturbances are amplified in the negative pressure rise region near the wing leading edge, while Tollmien–Schlichting (TS) waves (viscous instability of streamwise profiles) are amplified in the flat pressure region of the wing midchord. The possible interaction of these two types of disturbance may be quite significant in the successful design of laminar flow control wings.

Experimental investigations into the nature of the swept-wing boundary-layer instability, at its linear and nonlinear stage, have been carried out by Bippes and coworkers (see Bippes 1991; Müller & Bippes 1988; Müller 1989) at DLR, by Saric and coworkers (see Dagenhart *et al.* 1989; Saric, Dagenhart & Mousseux 1989; Kohama, Saric & Hoos 1991) at Arizona State University and by Arnal and coworkers (see Arnal & Juillen 1987) at ONERA/CERT. Experiments at DLR were performed on a swept-plate model with an imposed pressure gradient. A displacement body above the plate was used to generate the c_p distribution which varied almost linearly with chordwise distance. Saric and Arnal used infinite-swept aerofoils in their low-speed experiments.

Both stationary and travelling crossflow disturbances were observed in these experiments, as well as in the experiment of Poll (1985) on a swept cylinder. Müller & Bippes (1988) found that the stationary vortices, as well as travelling disturbances, reached nonlinear saturation in their experiment. However, they did not notice any explosive secondary instability leading to transition. On the other hand, Kohama *et al.* (1991) observed a high-frequency secondary instability prior to transition in their swept-wing experiment, where pressure gradient remained favourable ruling out any possibility of TS wave amplification. The frequency of this secondary instability was an order of magnitude higher than the frequency of the most-amplified travelling disturbance given by the linear theory. They concluded that, even though the travelling crossflow disturbances are observed, the transition process in this three-dimensional boundary layer is dominated by the stationary vortices and the associated secondary instability. Poll (1985) had also observed a high-frequency disturbance in his swept-cylinder experiment.

Müller & Bippes (1988) also studied the effect of free-stream turbulence on the instability behaviour in their experiment. They found that at 'low' levels (0.05%) of free-stream turbulence, stationary disturbances amplified to large amplitudes but these large amplitudes of the stationary vortices did not necessarily lead to early transition. The experiments performed in wind tunnels with higher turbulence levels (0.15 and 0.3%) showed weaker growth of stationary disturbances but earlier transition due to stronger travelling disturbances. They concluded that travelling waves, and not the stationary vortices, play the major role in the transition process. Their experimental results also seem to suggest an early nonlinear interaction between stationary and travelling crossflow disturbances.

Theoretical investigations into linear and nonlinear stability of three-dimensional boundary layers have been carried out by Balachandar, Streett & Malik (1992), Fischer & Dallmann (1991), Malik (1986), Meyer & Kleiser (1988) and Reed (1987). Fischer & Dallmann used secondary instability theory and Meyer & Kleiser used direct simulation of Navier–Stokes equations to study the swept-plate experiment of Müller & Bippes (1988). Fischer & Dallmann argued that the travelling disturbances observed in the DLR experiment are secondary disturbances of the mean flow modulated by the stationary vortices and should not be thought of as the primary instability of the three-dimensional boundary-layer flow. The direct numerical simulation of Meyer & Kleiser found nonlinear equilibrium states for stationary as well as travelling disturbances, in

agreement with the DLR experiment. Similar equilibrium states for stationary vortices were computed by Malik (1986) in rotating-disk boundary layer. Balachandar *et al.* (1992) performed a secondary instability analysis of the rotating-disk boundary layer where the stationary vortices constituted the primary instability. They were able to find a high-frequency secondary instability similar to the one observed by Kohama (1984, 1987) in a rotating-disk boundary layer.

All these experimental and theoretical investigations consider a class of mean flows that is only unstable to inflectional crossflow disturbances and do not support TS wave amplification. Results from various experiments appear to suggest that, for this class of flow, there are at least two possible scenarios for transition. If the free-stream turbulence level is very small, i.e. the initial amplitude of the non-stationary disturbances is small relative to the stationary disturbances which most certainly are introduced at local surface imperfections, then stationary disturbances dominate the initial stage of the disturbance growth leading to a high-frequency secondary instability resulting in final breakdown. When the initial amplitude of the travelling modes is not small, nonlinear interaction between these travelling modes and stationary vortices is present and the character of the final breakdown is influenced by the relative amplitudes of the stationary vortices and the travelling modes. The other class of flow, where TS waves could amplify, is also of technological importance but has not been studied either experimentally or theoretically.

The objective of this research is to study various wave-interaction mechanisms and laminar-flow breakdown in three-dimensional boundary layers. Previous linear and nonlinear theoretical investigations have been performed by using the parallel-flow approximation and have been local in nature. This study includes non-parallel effects and sets up the problem within the framework of nonlinear parabolized stability equations (PSE). Intermodal interaction and the effect of initial conditions can also be studied by using this approach. Basic insight into the physical mechanisms involved in swept-wing flow transition can be achieved by considering simple model flows. One such flow is the swept Hiemenz flow in which the interaction of stationary and travelling crossflow disturbances can be studied. In this paper we study linear and nonlinear crossflow disturbances as well as the interaction between stationary and travelling modes. We also study secondary instability of the three-dimensional mean flow modulated by the stationary vortices. Section 2 describes the basic flow for the swept Hiemenz problem and the associated PSE analysis is given in §3. The results for linear and nonlinear stability analysis and wave interactions are given in §4. Section 5 describes the results from secondary instability analysis and the conclusions are given in §6.

2. The swept Hiemenz problem

The flow past a circular cylinder, outside the viscous boundary layer, can be represented as

$$U_\infty = cx^* + c_1 x^{*3} + c_2 x^{*5} + \ldots, \tag{2.1}$$

where U_∞ is the velocity along the coordinate x^* and c, c_1, etc. are constants. In two-dimensional stagnation-point flow, only the first term in the series (2.1) is retained and, hence, the velocity U_∞ increases linearly with distance x^*, i.e.

$$U_\infty = cx^*. \tag{2.2}$$

If we consider the Cartesian coordinate system x^*, y^*, z^*, then (2.2) gives the far-field

($y^* \to \infty$) solution of the impinging flow on a plate along x^* which we define here by $y^* = 0$. The associated viscous problem was first investigated by Hiemenz who found an exact solution which is named after him. This stagnation flow was found to be stable to infinitesimally small disturbances propagating along z^* by Wilson & Gladwell (1978).

The swept Hiemenz problem is constructed by introducing a velocity component W_∞ along the z^* axis, which amounts to changing the inclination of the impinging stream with respect to z^*. The flow is symmetric about the line $x^* = 0$, which is called the attachment line. Linear and nonlinear stability of the attachment-line boundary layer has been studied by Hall, Malik & Poll (1984) and Spalart (1988). In this paper we study the stability of this flow for $x^* > 0$ as was recently done by Spalart (1989) using full Navier–Stokes equations.

2.1. *The basic flow*

We consider the flow of a viscous incompressible fluid of kinematic viscosity ν. Let $l = (\nu/c)^{\frac{1}{2}}$ be a typical thickness of the boundary layer which is used here as the lengthscale. We note that l is independent of x^*. Thus, we have the scaled coordinates x, y, z given as

$$(x, y, z) = (x^*/l, y^*/l, z^*/l).$$

We also define two Reynolds numbers R and $\bar{R}$:

$$R = U_\infty l/\nu, \tag{2.3}$$

$$\bar{R} = W_\infty l/\nu. \tag{2.4}$$

From (2.2) and (2.3), it follows that

$$R = x^*/l = x. \tag{2.5}$$

The local angle θ of the inviscid streamline, with respect to the x-axis, is given as

$$\theta = \arctan(W_\infty/U_\infty) = \arctan(\bar{R}/R). \tag{2.6}$$

We now look for a solution to the Navier–Stokes equations which satisfies the following conditions:

$$u^* = v^* = w^* = 0, \quad y^* = 0, \tag{2.7}$$

$$u^* \to U_\infty, \quad w^* \to W_\infty, \quad y^* \to \infty, \tag{2.8}$$

where u^*, v^*, w^* are velocity components in the x^*, y^*, z^* directions, respectively. It is convenient to define a stream function Φ so that

$$u^* = \partial\Phi/\partial y^*, \quad v^* = -\partial\Phi/\partial x^*$$

and

$$\Phi = x^*(c\nu)^{\frac{1}{2}} f(y).$$

If we use W_∞ as the velocity scale, then

$$\bar{u} = u^*/W_\infty = (x/\bar{R}) f'(y), \tag{2.9}$$

$$\bar{v} = v^*/W_\infty = -(1/\bar{R}) f(y). \tag{2.10}$$

Similarly,

$$\bar{w} = w^*/W_\infty = g(y), \tag{2.11}$$

where f and g are governed by the ordinary differential equations

$$f'''+ff''+(1-f'^2)=0, \tag{2.12}$$

$$g''+fg'=0, \tag{2.13}$$

where primes denote differentiation with respect to y.

The mean flow derivatives needed in the stability analysis below can be written as

$$\bar{u}_y=\frac{x}{\bar{R}}f'', \quad \bar{u}_{yy}=\frac{x}{\bar{R}}f''', \quad \bar{v}_y=-\frac{1}{\bar{R}}f', \quad \bar{v}_{yy}=-\frac{1}{\bar{R}}f'',$$

$$\bar{w}_y=g', \quad \bar{w}_{yy}=g'', \quad \bar{u}_x=(1/\bar{R})f'.$$

Numerical solution of (2.12) and (2.13) thus yields the mean flow and its derivatives without any additional approximation and the boundary-layer thickness does not vary with x.

3. PSE analysis for three-dimensional boundary layers

Parabolized stability equations (PSE) for linear and nonlinear disturbances in two-dimensional boundary layers have been used by Herbert (1991) and Bertolotti, Herbert & Spalart (1992) for incompressible flow where they used a stream-function formulation of the governing equations. In the present three-dimensional boundary-layer study, we follow the work of Chang *et al.* (1991) for compressible flow and formulate the incompressible stability problem using primitive variables in Cartesian coordinates x, y, and z. The basic flow is perturbed by fluctuations in the flow, i.e. the total field can be decomposed into a mean value (solution of (2.12) and (2.13)) and a perturbation quantity

$$u=\bar{u}+\tilde{u}, \quad v=\bar{v}+\tilde{v}, \quad w=\bar{w}+\tilde{w}, \quad p=\bar{p}+\tilde{p}, \tag{3.1}$$

where p is the pressure. Substituting (3.1) into the incompressible Navier–Stokes equations and subtracting from it the steady mean flow, we obtain the nonlinear disturbance equations as

$$\boldsymbol{\Gamma}\frac{\partial\boldsymbol{\phi}}{\partial t}+\boldsymbol{A}\frac{\partial\boldsymbol{\phi}}{\partial x}+\boldsymbol{B}\frac{\partial\boldsymbol{\phi}}{\partial y}+\boldsymbol{C}\frac{\partial\boldsymbol{\phi}}{\partial z}+\boldsymbol{D}\boldsymbol{\phi}-\left[\boldsymbol{E}_x\frac{\partial^2\boldsymbol{\phi}}{\partial x^2}+\boldsymbol{E}_y\frac{\partial^2\boldsymbol{\phi}}{\partial y^2}+\boldsymbol{E}_z\frac{\partial^2\boldsymbol{\phi}}{\partial z^2}\right]=\boldsymbol{F}, \tag{3.2}$$

where the left-hand side contains only linear operators operating on the disturbance vector $\boldsymbol{\phi}=(\tilde{u},\tilde{v},\tilde{w},\tilde{p})$ and the right-hand-side forcing vector $\boldsymbol{F}$ is due to nonlinear interaction and includes all nonlinear terms associated with the disturbances. The right-hand side is given as

$$\boldsymbol{F}=-\tilde{\boldsymbol{A}}\frac{\partial\boldsymbol{\phi}}{\partial x}-\tilde{\boldsymbol{B}}\frac{\partial\boldsymbol{\phi}}{\partial y}-\tilde{\boldsymbol{C}}\frac{\partial\boldsymbol{\phi}}{\partial z}. \tag{3.3}$$

In the above, $\boldsymbol{\Gamma}$ is the diagonal matrix [1, 1, 1, 0] while $\boldsymbol{A}$, $\boldsymbol{B}$, $\boldsymbol{C}$ are given as

$$\boldsymbol{A}=\begin{bmatrix}\bar{u}&0&0&1\\0&\bar{u}&0&0\\0&0&\bar{u}&0\\1&0&0&0\end{bmatrix}, \quad \boldsymbol{B}=\begin{bmatrix}\bar{v}&0&0&0\\0&\bar{v}&0&1\\0&0&\bar{v}&0\\0&1&0&0\end{bmatrix}, \quad \boldsymbol{C}=\begin{bmatrix}\bar{w}&0&0&0\\0&\bar{w}&0&0\\0&0&\bar{w}&1\\0&0&1&0\end{bmatrix},$$

and $\tilde{\boldsymbol{A}}, \tilde{\boldsymbol{B}}, \tilde{\boldsymbol{C}}$ are similar to $\boldsymbol{A}, \boldsymbol{B}, \boldsymbol{C}$ except that the overbars are replaced with tildes and all ones are dropped. The coefficient matrices $\boldsymbol{D}$, $\boldsymbol{E}_x$, $\boldsymbol{E}_y$, $\boldsymbol{E}_z$ are given as

$$\boldsymbol{D} = \begin{bmatrix} \bar{u}_x & \bar{u}_y & 0 & 0 \\ \bar{v}_x & \bar{v}_y & 0 & 0 \\ \bar{w}_x & \bar{w}_y & 0 & 0 \\ 0 & 0 & 0 & 0 \end{bmatrix},$$

$$\boldsymbol{E}_x = \boldsymbol{E}_y = \boldsymbol{E}_z = \begin{bmatrix} (1/\bar{R}) & 0 & 0 & 0 \\ 0 & (1/\bar{R}) & 0 & 0 \\ 0 & 0 & (1/\bar{R}) & 0 \\ 0 & 0 & 0 & 0 \end{bmatrix}.$$

We assume that the given disturbance is periodic in time and in the spanwise direction; thus, the disturbance function $\boldsymbol{\phi}$ can be expressed by the following Fourier series:

$$\boldsymbol{\phi} = \sum_{m=-\infty}^{\infty} \sum_{n=-\infty}^{\infty} \chi_{mn}(x, y)\, \mathrm{e}^{\mathrm{i}(n\beta z - m\omega t)}. \tag{3.4}$$

Here, the frequency ω and wavenumber β are chosen such that the longest period and wavelength are $2\pi/\omega$ and $2\pi/\beta$ in the temporal and spanwise domains, respectively. For most stability problems of interest, it is sufficient to truncate (3.4) to only a finite number of modes

$$\boldsymbol{\phi} = \sum_{m=-M}^{M-1} \sum_{n=-N}^{N-1} \chi_{mn}(x, y)\, \mathrm{e}^{\mathrm{i}(n\beta z - m\omega t)}, \tag{3.5}$$

where M and N represent one-half the number of modes kept in the truncated Fourier series. Substituting (3.5) in (3.2) we obtain governing equations for χ_{mn} which are elliptic. In order to facilitate the solution of these equations we decompose the disturbance into a fast-varying wave-like part and a slowly varying shape function and write χ_{mn} as

$$\chi_{mn}(x, y) = \Psi_{mn}(x, y)\, \mathscr{A}_{mn}(x), \tag{3.6a}$$

$$\mathscr{A}_{mn}(x) = \exp\left[\mathrm{i} \int_{x_0}^{x} \alpha_{mn}(\xi)\, \mathrm{d}\xi\right], \tag{3.6b}$$

where Ψ_{mn} is the shape function ($\hat{u}_{mn}, \hat{v}_{mn}$, etc.) for the Fourier mode $(m\omega, n\beta)$ and α_{mn} is the associated streamwise (complex) wavenumber. With a proper choice of α_{mn} in (3.6b), the arbitrariness in (3.6a) can be removed and the equations for Ψ_{mn} can be parabolized. In other words, α_{mn} is chosen such that variation of Ψ_{mn} with x is minimized which allows the approximation $\partial^2 \Psi_{mn}/\partial x^2 = 0$. The PSEs for the shape function of a single Fourier mode (m, n) can be written as

$$\bar{\boldsymbol{G}}_{mn}\, \Psi_{mn} + \bar{\boldsymbol{A}}_{mn} \frac{\partial \Psi_{mn}}{\partial x} + \bar{\boldsymbol{B}}_{mn} \frac{\partial \Psi_{mn}}{\partial y} = \boldsymbol{E}_y \frac{\partial^2 \Psi_{mn}}{\partial y_2} + \boldsymbol{F}_{mn}/\mathscr{A}_{mn}, \tag{3.7}$$

where matrices $\bar{\boldsymbol{G}}_{mn}$, $\bar{\boldsymbol{A}}_{mn}$ and $\bar{\boldsymbol{B}}_{mn}$ are given by

$$\bar{\boldsymbol{G}}_{mn} = -\mathrm{i}m\omega \boldsymbol{\Gamma} + \mathrm{i}\alpha_{mn} \boldsymbol{A} + \mathrm{i}n\beta \boldsymbol{C} + \boldsymbol{D} - \boldsymbol{E}_x \left(\mathrm{i} \frac{\mathrm{d}\alpha_{mn}}{\mathrm{d}x} - \alpha_{mn}^2\right) + n^2 \beta^2 \boldsymbol{E}_z,$$

$$\bar{\boldsymbol{A}}_{mn} = \boldsymbol{A} - 2\mathrm{i}\alpha_{mn} \boldsymbol{E}_x,$$

$$\bar{\boldsymbol{B}}_{mn} = \boldsymbol{B}.$$

The nonlinear forcing function F_{mn} is the Fourier component of the total forcing, $\boldsymbol{F}$, and can be evaluated by the Fourier series expansion

$$\boldsymbol{F}(x,y,z,t) = \sum_{m=-M}^{M-1} \sum_{n=-N}^{N-1} F_{mn}(x,y)\, \mathrm{e}^{\mathrm{i}(n\beta z - m\omega t)}. \tag{3.8}$$

The Fourier decomposition of (3.8) can be done by using the fast fourier transform (FFT) of $\boldsymbol{F}$, which is evaluated numerically in the physical space.

The PSEs (3.7) can be used to study nonlinear interaction of various modes (e.g. crossflow/crossflow, crossflow/TS, etc.) or one can study the onset of transition to turbulence provided appropriate initial conditions are prescribed. For small disturbances, $\boldsymbol{F}$ can be neglected and one obtains linear PSEs (after dropping the subscript 11),

$$\bar{\boldsymbol{G}}\Psi + \bar{\boldsymbol{A}}\frac{\partial \Psi}{\partial x} + \bar{\boldsymbol{B}}\frac{\partial \Psi}{\partial y} = \boldsymbol{E}_y \frac{\partial^2 \Psi}{\partial y^2}, \tag{3.9}$$

which can be solved to study the effect of non-parallel flow or that of initial conditions. If the non-parallel effect is ignored, then (3.9) essentially reduces to the Orr–Sommerfeld equation.

The streamwise wavenumber in (3.6*b*) needs to be determined in order to solve the equations by a marching scheme. This procedure is given in Chang *et al.* (1991). Here we briefly describe it for the linear equation (3.9). In this case, the evolution of the shape function is monitored during the process of marching and the wavenumber is updated by local iterations at a given x according to the change in Ψ. At a given location x_1, let the streamwise wavenumber be given by α_1 and then express $\boldsymbol{\phi}$ as

$$\boldsymbol{\phi}(x,y,z,t) = \Psi(x,y)\exp\left[\mathrm{i}\left(\int_{x_1}^{x} \alpha_1 \,\mathrm{d}\xi + \beta z - \omega t\right)\right]. \tag{3.10}$$

The change of the shape function Ψ can be approximated by the following Taylor series expansion truncated to the first order

$$\Psi(x,y) = \Psi_1 + \frac{\partial \Psi_1}{\partial x}(x - x_1) + \ldots,$$

where Ψ_1 is the shape function at $x = x_1$. To an accuracy of $O(x - x_1)$, the above equation can be further expressed as

$$\Psi(x,y) = \Psi_1 \exp\left[\int_{x_1}^{x} \frac{1}{\Psi_1}\frac{\partial \Psi_1}{\partial x}\,\mathrm{d}\xi\right]. \tag{3.11}$$

Substituting (3.11) into (3.10), we have the 'effective' wavenumber in the vicinity of x_1 given by

$$\alpha = \alpha_1 - \mathrm{i}\frac{1}{\Psi_1}\frac{\partial \Psi_1}{\partial x}. \tag{3.12}$$

The real part of this effective wavenumber represents the phase change of the disturbance while the imaginary part gives the growth rate. A disturbance is unstable if the imaginary part is less than zero. Since the shape function vector Ψ_1 depends upon y and contains four dependent variables ($\hat{u}, \hat{v}$, etc.), the value of α computed by (3.12) will be a function of the y-coordinate and the selected dependent variable. One can, for example, use the shape function $\hat{u}$ and the y location where $\hat{u}$ reaches its local maximum

to update the wavenumber at any given x-station as the disturbance evolves downstream. An alternative which is used here is to consider the following integral condition:

$$\alpha_{new} = \alpha_{old} - \mathrm{i} \int q^{\dagger} \frac{\partial q}{\partial x} \mathrm{d}y \Big/ \int |q|^2 \, \mathrm{d}y, \tag{3.13}$$

which removes the dependence of α on y. If q is a particular component of Ψ_1 then the dependence of α on Ψ_1 is retained in (3.13). For three-dimensional boundary layers we choose q to be a vector with components $(\hat{u}, \hat{v}, \hat{w})$. Equation (3.13) is used in the iterative solution of (3.9) until the second term in (3.13) vanishes to a prescribed tolerance. An additional condition (Chang *et al.* 1991; Malik & Li 1993) needs to be satisfied in order to obtain solution of (3.7) by the space marching approach.

Numerical solution of the parabolized stability equations requires discretization in both the x- and y-directions. We discretize the streamwise derivative by a backward Euler step and wall-normal derivatives by fourth-order-accurate compact differences (see Malik, Chuang & Hussaini 1982). Homogeneous boundary conditions at the wall and in the free stream are imposed. The initial conditions are obtained by a local approximation to (3.9) and by solving the associated eigenvalue problem. Since the wave information is absorbed in the wavenumber α (3.6*b*), one needs to use a few marching steps per wavelength to obtain an accurate solution of the wave evolution. Calculations for two-dimensional boundary layers show that PSE results with only three steps per wavelength agree quite well with very accurate Navier–Stokes computations using 60 grid points per wavelength (see Joslin, Streett & Chang 1992).

4. Linear and nonlinear stability analysis and wave interaction

4.1. *Quasi-parallel linear stability*

In order to determine the relevant physical parameter space, it is appropriate to first give some results from quasi-parallel linear stability theory. We consider two cases: $\bar{R} = 250$ and 500. Hall *et al.* (1984) found that the attachment-line boundary layer ($x = 0$) is stable to infinitesimal disturbances up to $\bar{R} = 583.1$. Thus, for the two cases considered here, the attachment-line boundary layer is stable. In the present study, we are interested in the crossflow disturbances that will become unstable away from the attachment-line ($x \gg 1$). Figure 1 shows the mean velocity profiles in directions tangential and across the inviscid stream at $R = 500$ and $\bar{R} = 500$. The velocity profiles U_t and U_c are defined as

$$U_t = \bar{u} \cos\theta + \bar{w} \sin\theta,$$

$$U_c = \bar{u} \sin\theta - \bar{w} \cos\theta,$$

where the streamline angle θ is defined in (2.6). These velocity profiles have been scaled with spanwise inviscid velocity W_{∞}. It is clear from (2.6) that θ decreases with R or x as the flow turns away from the attachment line towards the free-stream direction. This is depicted in figure 2 where the angle θ, along with the crossflow Reynolds number R_{cf} (defined below), is plotted for $\bar{R} = 250$ and 500.

Crossflow instability is associated with the inflectional velocity profile U_c which, for swept wings, is positive towards the centre of curvature of the streamline. The flow becomes unstable when crossflow Reynolds number $R_{cf} \geqslant 40$, where R_{cf} is defined by

$$R_{cf} = \bar{U}_c \delta_{0.1} / \nu, \tag{4.1}$$

where $\bar{U}_c$ is the maximum value of the crossflow velocity U_c and $\delta_{0.1}$ is the thickness

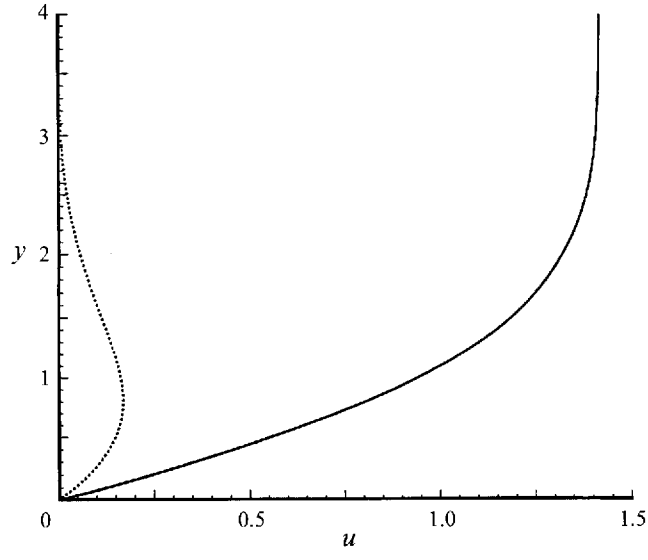

FIGURE 1. Streamwise U_t (——) and crossflow U_c (· · · · · ·) velocity profiles in the swept-Hiemenz flow. $R = \bar{R} = 500$.

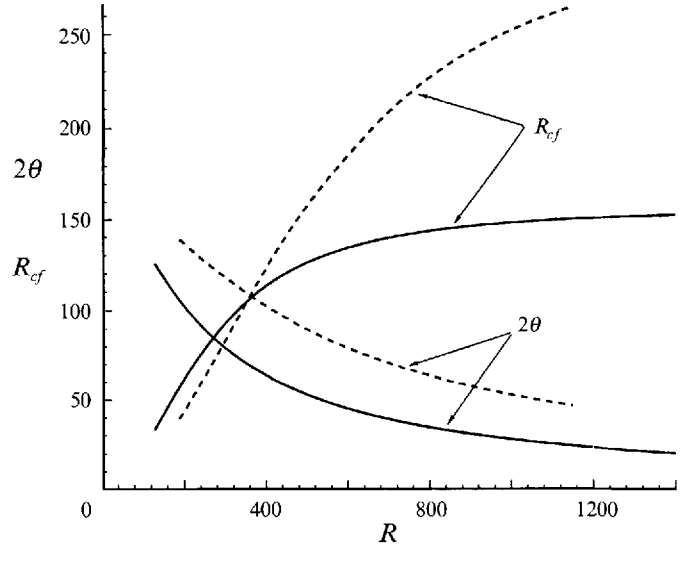

FIGURE 2. Variation of inviscid streamline angle (θ) and crossflow Reynolds number (R_{cf}). ——, $\bar{R} = 250$; – – –, $\bar{R} = 500$.

where the crossflow velocity has dropped to 10% of $\bar{U}_e$. The distribution of the crossflow Reynolds number R_{cf} is given for the two cases in figure 2. The value of R_{cf} exceeds about 50 at $R = 200$ and, hence, the instability will onset at $R < 200$ for both cases. The maximum value of R_{cf} is about 150 for $\bar{R} = 250$ and about 270 for $\bar{R} = 500$. In swept-wing flows, transition usually occurs where R_{cf} becomes of $O(200)$.

Figure 3 presents results for integrated growth,

$$\ln(A/A_0) = \int_{R_c}^{R} \sigma_p \, \mathrm{d}R, \tag{4.2}$$

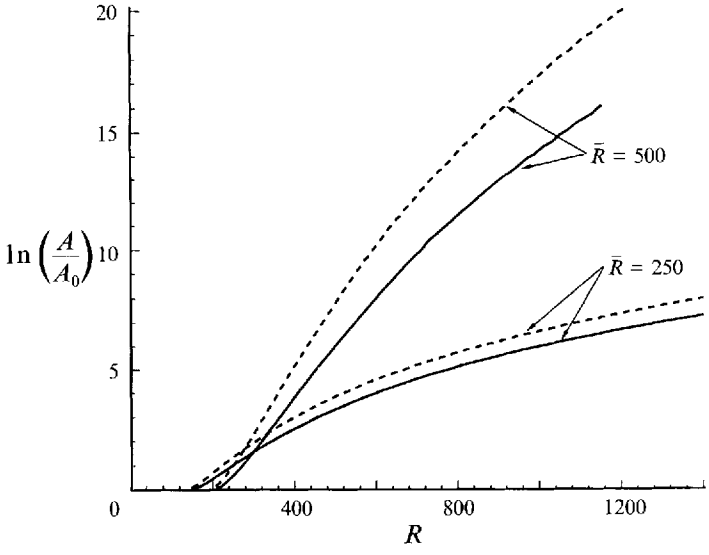

FIGURE 3. Integrated growth for fixed spanwise wavenumber $\beta = 0.4$. ——, $F = 0$; – – –, $F = 0.75 \times 10^{-4}$.

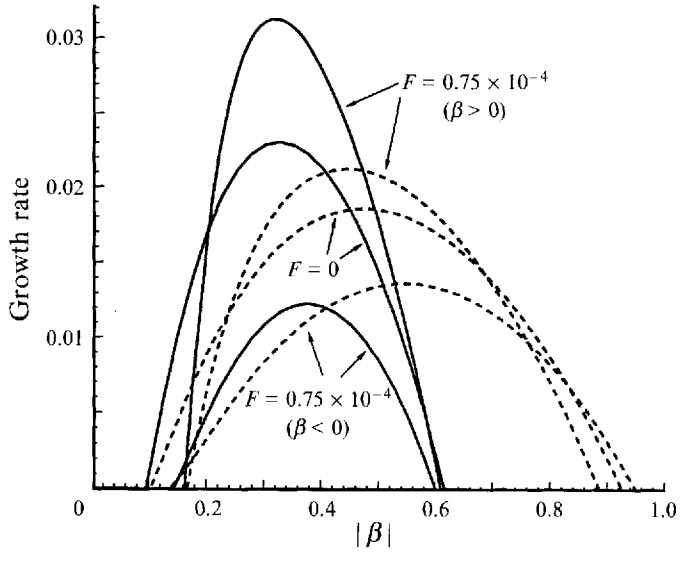

FIGURE 4. Quasi-parallel growth rate for positive and negative β at $\bar{R} = 500$. ——, $R = 300$; – – –, $R = 650$.

using the quasi-parallel growth rate $\sigma_p = -\alpha_i$. Calculations are performed for stationary as well as travelling disturbances with frequency $F = 0.75 \times 10^{-4}$ (where $F = 2\pi\nu f / W_\infty^2$, f being the frequency in Hertz) at both $\bar{R}$. These calculations are performed for a fixed spanwise wavenumber of 0.4 which is close to, but not quite (see figure 4 below), the most-amplified wavenumber for the flow under study. It is clear that travelling disturbances amplify more than the stationary disturbances according to linear theory. However, stationary disturbances are found to dominate when experiments are performed in low-disturbance wind tunnels. This is due to the lower

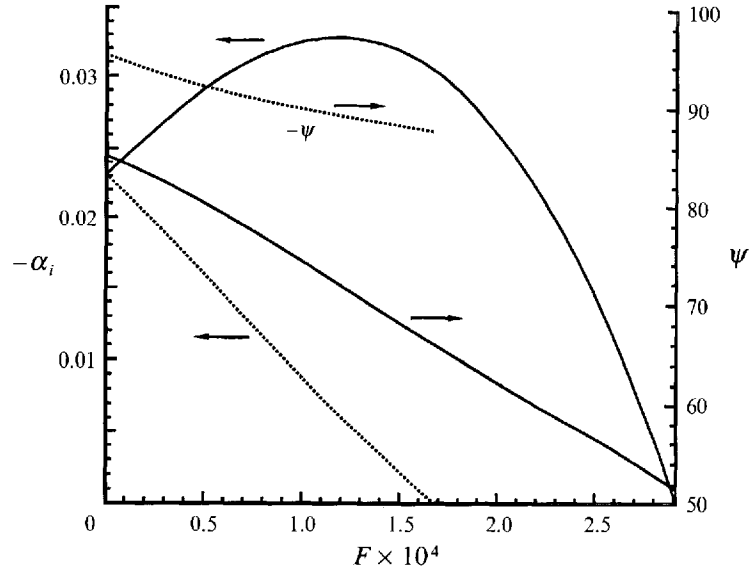

FIGURE 5. Growth rates (most amplified) and orientation (ψ) of the two families of unstable modes at $\bar{R} = 500$, $R = 300$.

initial amplitude of travelling modes (see the work of Choudhari & Streett 1990 on the receptivity of stationary and travelling disturbances).

The variation of spatial growth rate with wavenumber β is given in figure 4 for the two frequencies. There are two curves associated with $F = 0.75 \times 10^{-4}$, one with positive β and another with negative β, the latter with smaller growth rates. The stationary vortex and $\beta > 0$ travelling disturbance has peak growth rate at $\beta \approx 0.35$ as shown in the figure for $R = 300$. Downstream, the peak shifts to higher wavenumbers and lies, for example, at $\beta \approx 0.45$, $R = 650$. The two families of unstable travelling disturbances are again shown in figure 5 where the growth rate of the most-amplified (among various wave orientations) disturbance is plotted as a function of frequency. The family with high growth rates has its wave vector oriented at positive angles with respect to the inviscid flow streamline (angles measured from the convex side) while the family with lower growth rates has its wave vector oriented at negative angles. The relative sense of the two modes depends upon the direction of the crossflow with the more-amplified mode always oriented opposite to the crossflow direction. In both cases, the direction of the group velocity lies at small angles to the inviscid streamline direction. Thus, the disturbance energy propagates downstream for both modes as also noted by Mack (1985). The travelling mode with lower growth rate may be important in the nonlinear stage and its interaction with the more amplified travelling mode may also induce stationary crossflow vortices when other stimuli, e.g. wall roughness, are absent. Furthermore, these two travelling modes along with stationary vortex mode constitute a possible resonant triad which may be relevant in the transition process.

4.2. *Non-parallel effects*

We now compare the quasi-parallel growth rate results with those obtained by solving linear PSEs, (3.9). Figure 6(*a*) shows the results for $\bar{R} = 250$ for stationary vortices while figure 6(*b*) shows the results for a frequency of $F = 0.75 \times 10^{-4}$. In case of PSEs, different growth rate results are obtained for the $\hat{u}$-, $\hat{v}$- and $\hat{w}$-components of velocity.

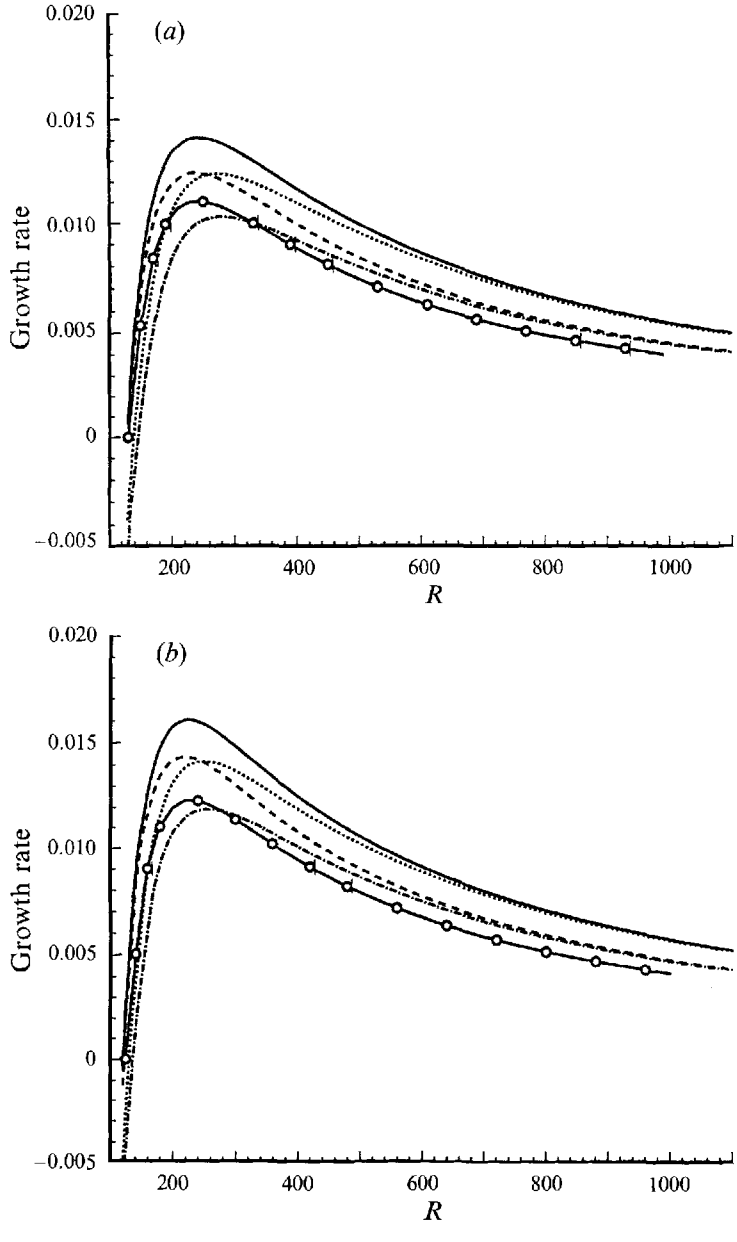

FIGURE 6. Disturbance growth rate for $\beta = 0.4$ and $\bar{R} = 250$: (*a*) stationary vortex, (*b*) travelling disturbance with frequency $F = 0.75 \times 10^{-4}$. ——, Based on max ($\hat{u}$); – – –, based on max ($\hat{v}$); – · – · –, based on max ($\hat{w}$); · · · · · ·, based on energy; —○—, parallel calculation.

At low R (between 200 and 400) there is a considerable difference between these growth rates with $\hat{u}$ growth higher than $\hat{v}$ and $\hat{w}$ but the latter two approach the same value at higher Reynolds numbers. Figure 7 shows the growth rate results for $\bar{R} = 500$. In this case the qualitative trends are the same but there is less difference between the three components. The quasi-parallel growth rate is, in general, close to the growth rate based upon the $\hat{w}$-component, except at lower Reynolds numbers where it lies somewhere in between the three growth rates. Thus, one cannot make a strong

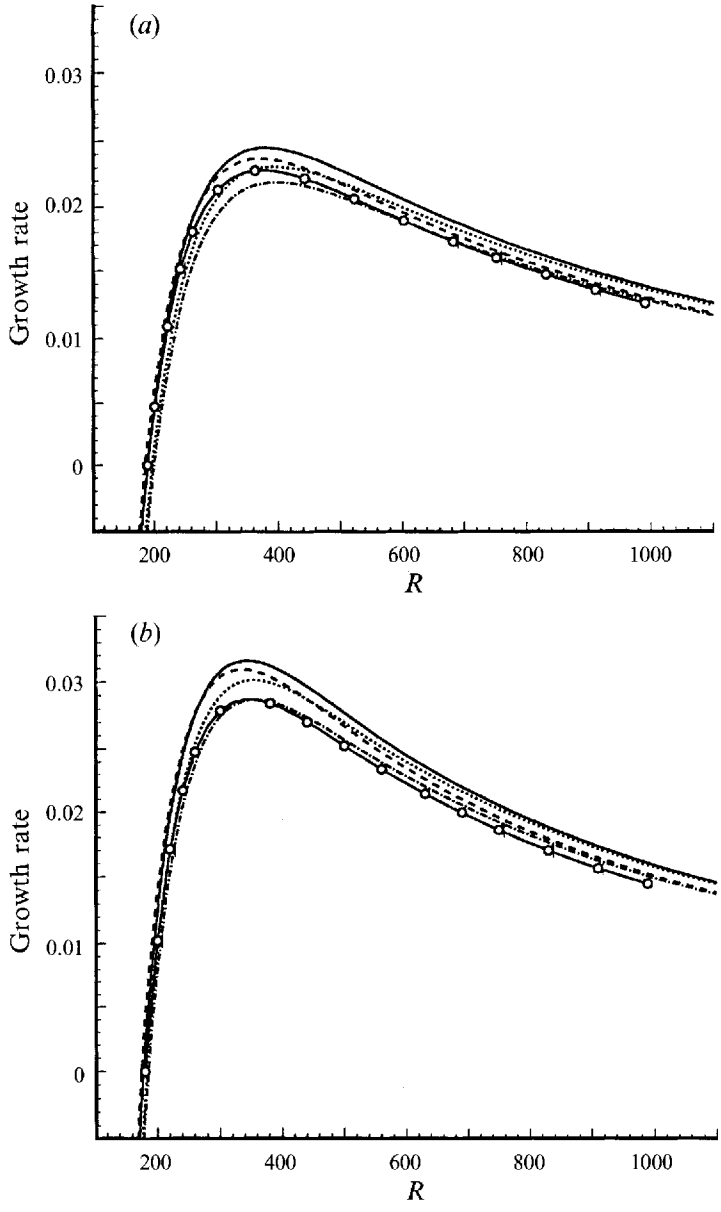

FIGURE 7. As figure 6 but for $\bar{R} = 500$.

statement about non-parallel effects except that they are more pronounced at lower $\bar{R}$ and that they are destabilizing if measured by the chordwise velocity component. The growth rate can also be defined based upon the total disturbance energy which accounts for all the velocity components and growth rates based upon this definition suggests that non-parallel effect is usually destabilizing, but there may be some exceptions. Spalart (1989) pointed out that the growth rates from his simulation were very close to the quasi-parallel results and that the agreement was better at lower Reynolds numbers (R) than at higher Reynolds numbers. Figure 7(a) shows that this is true for the case he considered ($\bar{R} = 500$, $F = 0$), but it is not a general statement as is evident from the comparison of figures 6 and 7.

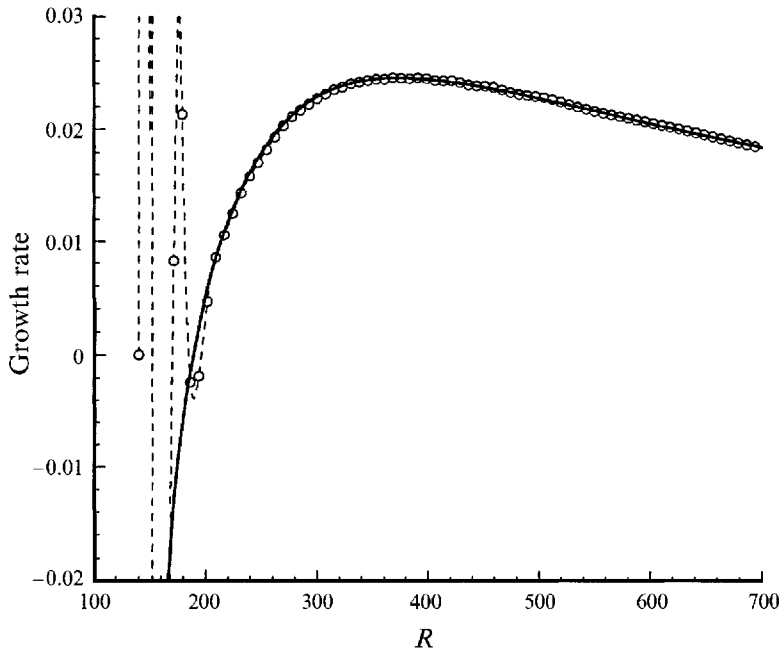

FIGURE 8. Comparison of linear PSE (——) and Navier–Stokes simulations of Streett (personal communication 1993) (---○---) for stationary vortex. ($\bar{R} = 500$, $\beta = 0.4$, growth rate based on $\hat{u}$).

Our results for $\beta = 0.4$ and $\bar{R} = 500$ are compared to the linearized Navier–Stokes computation of C. Streett (1993, personal communication) in figure 8. Streett performed spatial simulations and solved the full linearized system where the disturbances were introduced by spanwise-periodic steady suction and blowing. After the initial transients die out, the agreement between the two calculations is excellent and it remains so for a large chordwise extent. Good agreement was also found with the results of Spalart (1989) (see Malik & Li 1992). The agreement with the full Navier–Stokes solution shows that the PSE approximation introduces negligible error in our study of the crossflow vortices as disturbance growth rate is a sensitive quantity and any error would have shown up in growth rate results.

4.3. *Nonlinear development of stationary crossflow vortices*

Navier–Stokes simulations by Malik (1986) for rotating-disk flow and by Meyer & Kleiser (1988) for a Falkner–Skan–Cooke boundary layer showed nonlinear saturation of crossflow vortices. Both these calculations employed a temporal approach and, therefore, ignored non-parallel effects. Here we present spatial nonlinear calculations for $\bar{R} = 500$ using PSEs. Initial conditions for the stationary vortex with $\beta = 0.4$ were prescribed at $R = 186$. It was assumed that the vortex shape is given by the linear eigenfunction at that Reynolds number and that the maximum disturbance amplitude $(\max(\hat{u}^2 + \hat{w}^2)^{\frac{1}{2}})$ is $0.001\,W_\infty$. Figure 9 gives the computed total perturbation wall vorticity distribution

$$\left(\left(\frac{\partial u}{\partial y}\right)^2 + \left(\frac{\partial w}{\partial y}\right)^2\right)^{\frac{1}{2}} - \left(\left(\frac{\partial \bar{u}}{\partial y}\right)^2 + \left(\frac{\partial \bar{w}}{\partial y}\right)^2\right)^{\frac{1}{2}},$$

which shows streamwise striations starting at $R = 350$. The green colour indicates

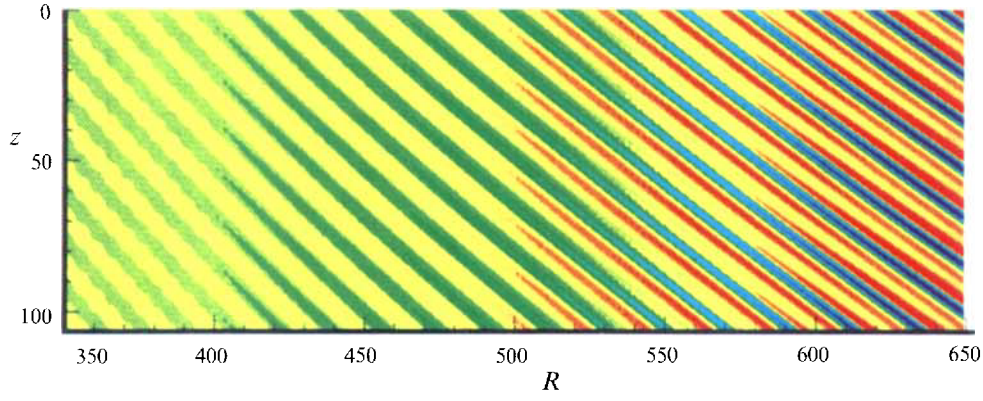

FIGURE 9. Computed wall vorticity distribution in the presence of nonlinear stationary vortices, $\beta = 0.4$, $\bar{R} = 500$.

negative values while the red indicates positive. The perturbation wall vorticity values are very small initially and the signal becomes noticeable (strong) only at $R \approx 420$. As we will show later, the disturbance amplitude at this location has already reached about 4%. Hence, when these vortices are observed in a flow visualization experiment it is almost certain that they have entered the nonlinear stage with growth rates somewhat smaller than that given by the linear theory. These striations are evident in almost all crossflow experiments (Gray 1952; Gregory *et al.* 1955; Poll 1985; Saric *et al.* 1989) and result from variation in the wall shear caused by stationary vortices. These vortices make a small angle (4–5°) with respect to the inviscid free stream.

Figure 10 shows the contours of the u-velocity in the (y, z)-plane at various Reynolds numbers ($R = 400$, 500, 600 and 650). Two spanwise wavelengths are shown and the y-coordinate has been stretched for clarity. Crossflow vortices appear to result in a half-mushroom-like structure which is shown exaggerated in the figure. The actual structure is much more flat as shown in figure 11, drawn to scale. Initially the boundary-layer thickness is constant in z; however, as the crossflow instability rolls up into vortices, there appear regions of low and high velocity and, therefore, the boundary-layer thickness varies considerably in the span as, for example, seen for $R = 600$. In this case the variation is as much as by a factor of about 4.

There is a region near $z = 10$ and 25 (for $R = 600$) where the fluid is pushed towards the wall, while it is pushed away from the wall near $z = 5$ and 20. It is these low-velocity regions at $z = 5$ and 20 where oil accumulates in a flow visualization experiment resulting in wall streaks such as those shown in figure 9. The half-mushroom structure observed in figure 10 is the result of the asymmetry induced by the crosswind. In two-dimensional flow over a concave wall which is subject to centrifugal instability, a full mushroom structure appears as experimentally observed by Swearingen & Blackwelder (1987) and Peerhossaini & Wesfreid (1988).

Figure 12 shows a velocity vector plot in the (y, z)-plane at fixed R of 650. The velocities have been projected onto a cross-section normal to the vortex axis. An insight into the crossflow vortex structure may be achieved by releasing dye particles at some location within the flow field and following their paths as they are carried through the fluid in the (y, z)-plane. Two particles are injected at about $z = 22$; one is released very near the wall and the other at $y = 1.7$. The latter particle rolls into a big vortex centred at about $y = 2.5$ and $z = 12$. This is the primary crossflow vortex. There is a second tiny vortex near the wall centred at about $y = 1$ and $z = 8$ to which the particle released

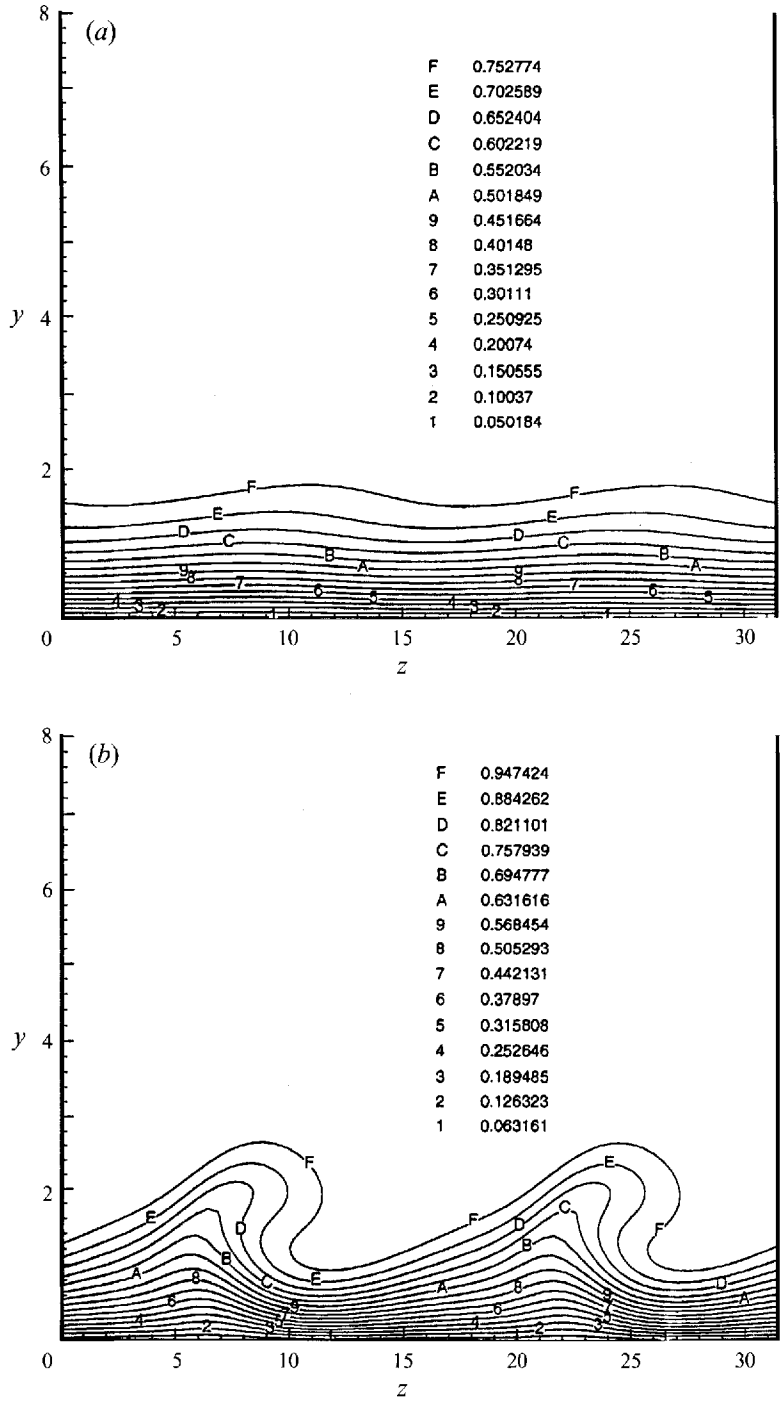

FIGURE 10(*a*, *b*). For caption see facing page.

near the wall is attracted. This second vortex which was much weaker at $R = 600$ has also been observed by R.-S. Lin (personal communication, 1992) in his Navier–Stokes simulations of the crossflow vortex on a swept wing. It should be stressed, however, that the actual flow is fully three-dimensional and varies along x. Hence, these particle

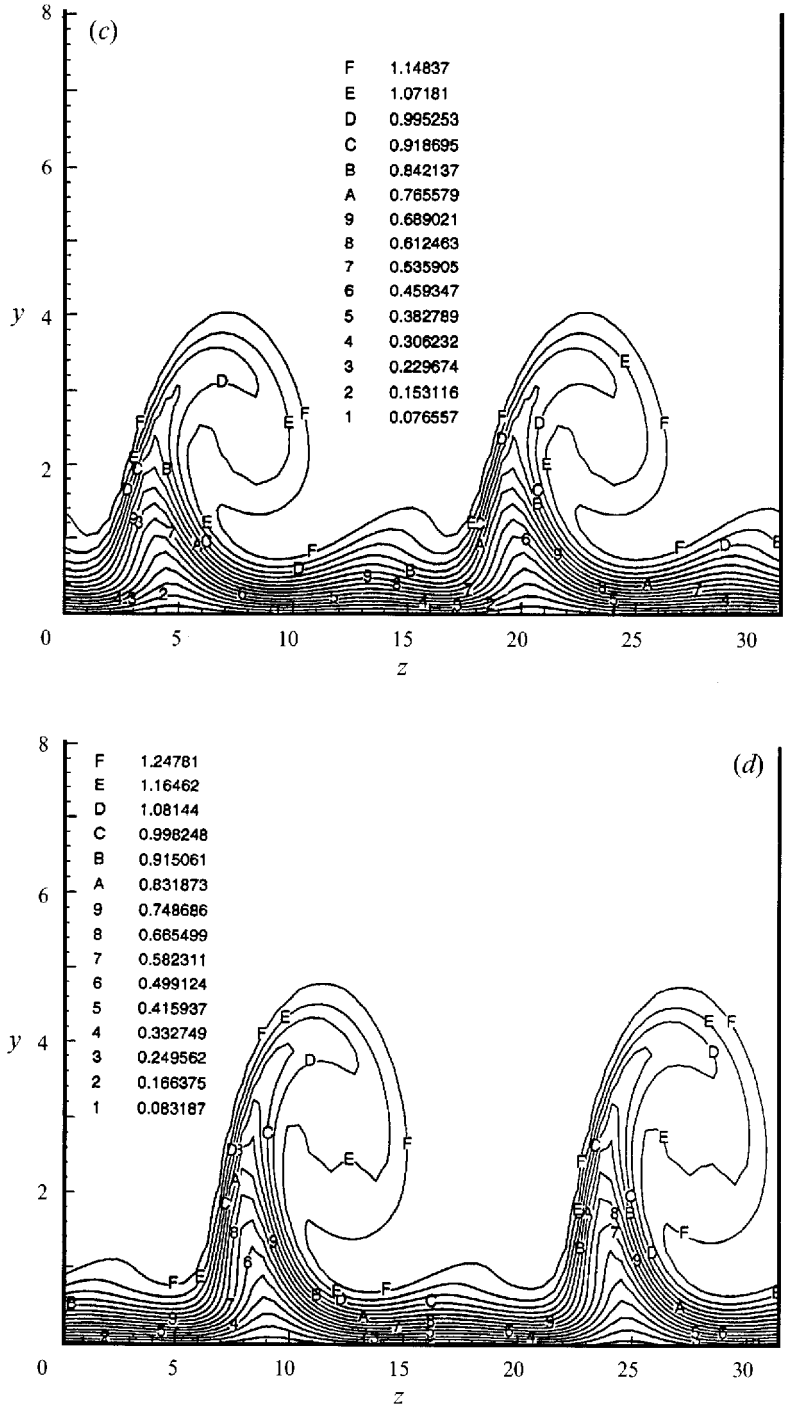

FIGURE 10. Variation of the u-velocity (for $\bar{R} = 500$) in the (y, z)-plane in the presence of a stationary crossflow vortex. Two spanwise wavelengths are shown. The view is from upstream. (*a*) $R = 400$, (*b*) $R = 500$, (*c*) $R = 600$, (*d*) $R = 650$.

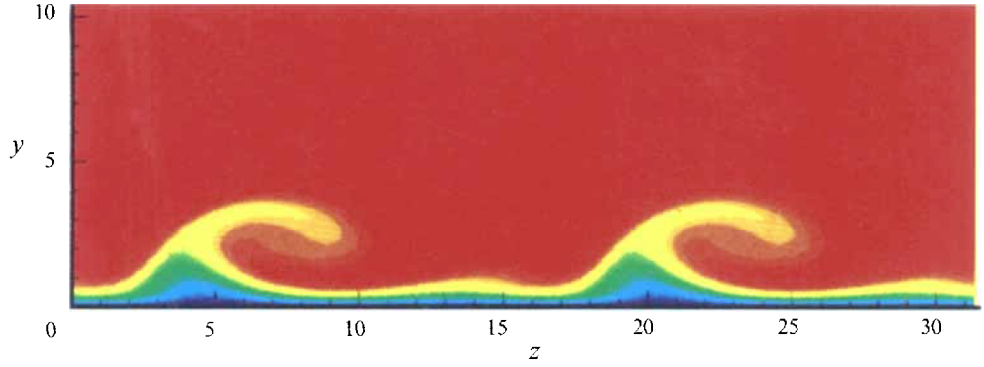

FIGURE 11. The structure of the crossflow vortex as viewed from upstream.

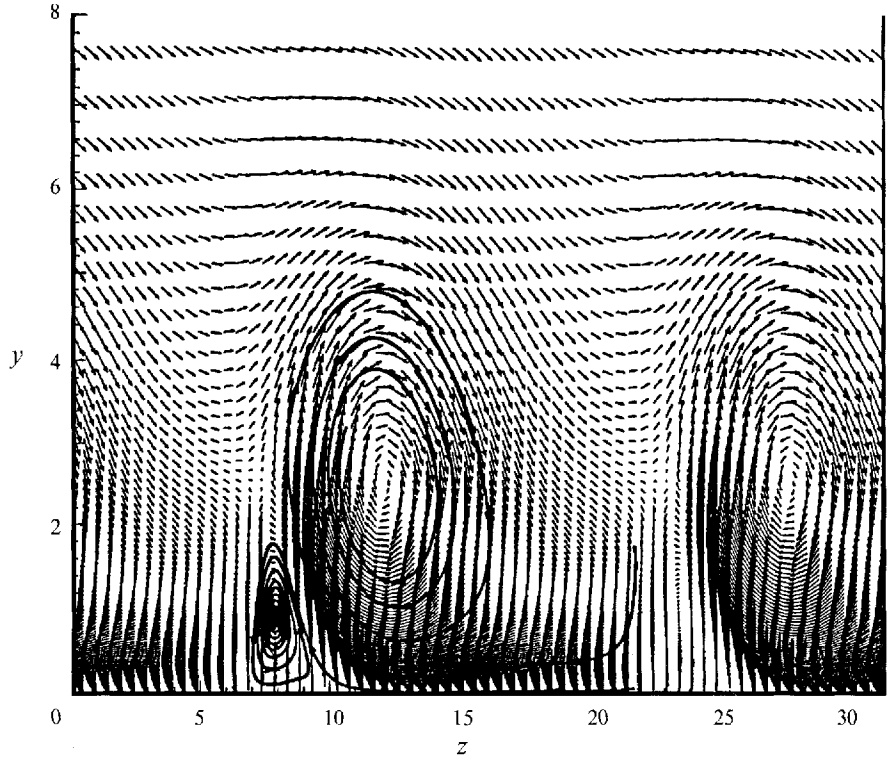

FIGURE 12. Velocity vector plot at $R = 650$ projected onto a plane perpendicular to the vortex axis.

traces do not depict the three-dimensional physical picture and have been used merely to facilitate the visualization of the crossflow vortices.

Contours in figure 10(*c*) show a second low-velocity region near $z = 15$ and 30; a hot wire located at $y = 1$, for example, will show two velocity defects per wavelength when traversed in the spanwise direction. This is depicted in figure 13 which shows that the second defect, caused by the 2β mode and sometimes referred to as vortex doubling, is much smaller than that caused by the main vortex. In our simulations, the 2β mode is excited through nonlinear interaction and its amplitude remains smaller than the primary mode with wavenumber β as shown in figure 14 where the amplitude functions

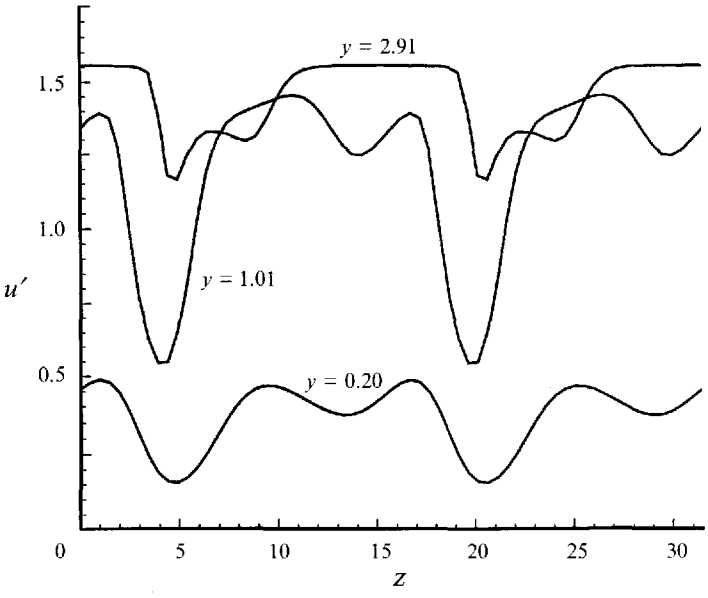

FIGURE 13. Variation of vortex axial velocity in the spanwise direction at $R = 600$.

for the stationary vortex along with its harmonics and mean flow correction are plotted at $R = 600$. In a laboratory experiment, the 2β mode may be excited via surface imperfections and the relative amplitudes of 1β and 2β modes may be different from the present case. The disturbance amplitude at $R = 600$ has reached to about 30% (when scaled with W_{∞}) with the maximum meanflow correction of about 15%. In a laboratory experiment, this picture will be altered owing to possible secondary instabilities and interaction with travelling modes.

Figure 15 shows the velocity profile along the crossflow vortex at four different locations across it for $R = 500$. The base flow given by the Hiemenz problem is also included. It can be seen that these profiles become strongly inflectional owing to the motion within the crossflow vortex. Such profiles were also noted in the swept-wing experiments of Dagenhart *et al.* (1989) and Müller & Bippes (1988). These inflectional profiles as well as the inflectional profiles in z (figure 13) are subject to inviscid secondary instabilities which are most likely related to the high-frequency disturbances observed by Kohama *et al.* (1991). We will investigate this aspect of the problem in a later section. Here, we first consider the interaction of travelling and stationary crossflow disturbances.

4.4. *Stationary and travelling wave interaction*

It was pointed out that the experiment of Müller & Bippes (1988) suggests an early nonlinear interaction between stationary and travelling waves. We now consider such interactions in the swept-Hiemenz flow. Our calculations are performed using $\beta = 0.4$ for both the stationary and travelling ($F = 0.75 \times 10^{-4}$) disturbances. The initial conditions were imposed at $R = 186$ and the amplitude of the stationary wave was the same as in §4.3 above, i.e. 0.1%. For travelling waves, two different initial amplitudes were considered: 0.01% and 0.1%. Results for both the cases are discussed below.

Figure 16 gives the disturbance energy of various modes denoted as (0, 1), (1, 1), (2, 2), etc. Here, the first index refers to frequency ω and the second index to spanwise wavenumber β. Thus, mode (2, 2) is the harmonic with twice the frequency and twice

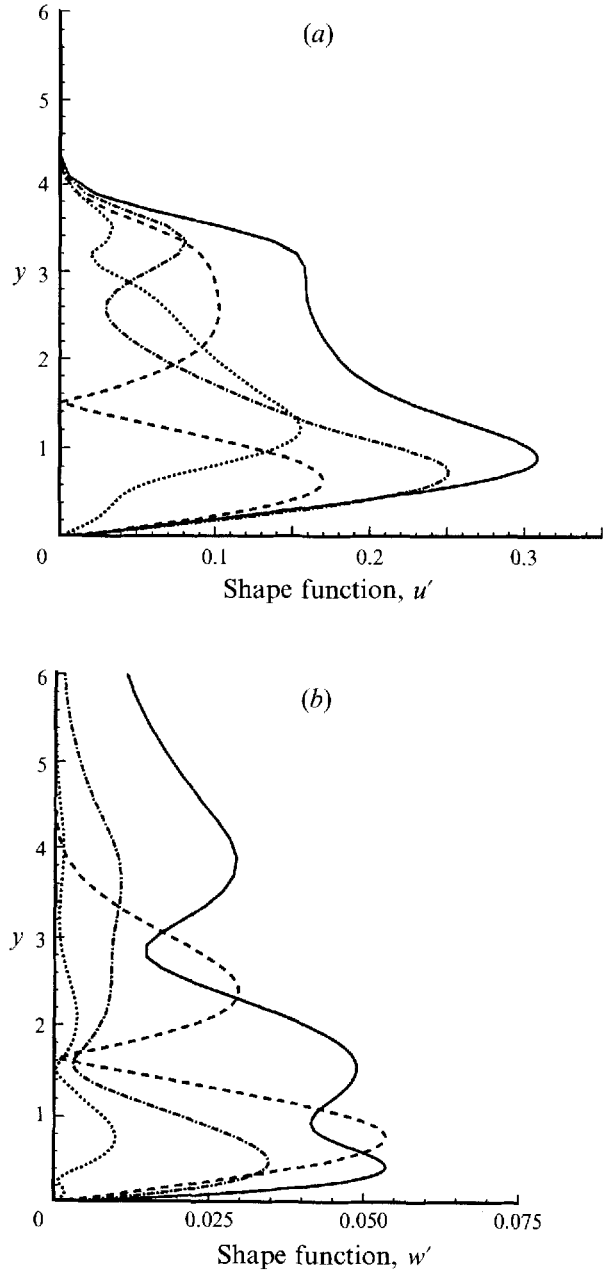

FIGURE 14. Disturbance amplitude functions for the stationary vortex (mode 1) and its harmonics, at $R = 600$, (*a*) along the vortex, (*b*) across the vortex. ---, Mode 0; ——, mode 1; –·–·–, mode 2; · · · · · ·, mode 3.

the wavenumber of the travelling mode. For comparison, the case of stationary vortex only is also given. For the stationary vortex case, shown in figure 16(*a*), the energy cascades into 2β, 3β, 4β... modes as earlier noted in the simulations by Malik (1986) and Meyer & Kleiser (1988). The energy in the mean flow correction mode is of the same order as the 2β mode. It is probable that the essential features of the nonlinear

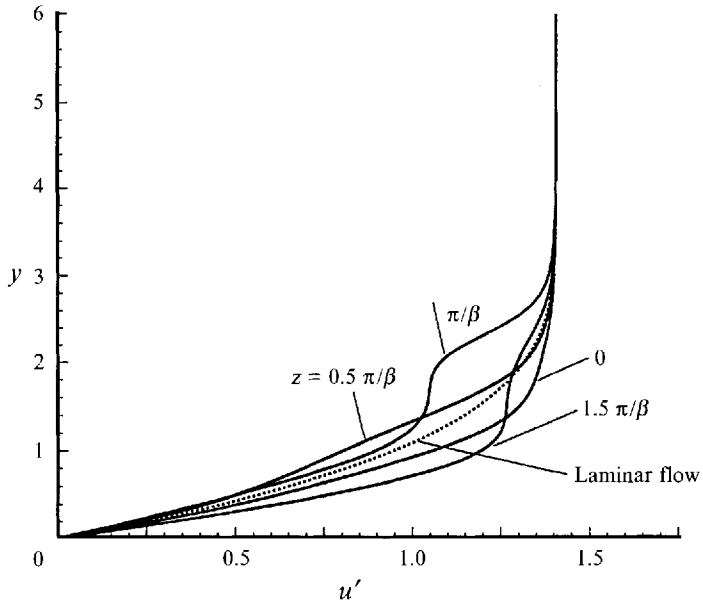

FIGURE 15. Velocity component along the vortex at different locations z across the vortex, $R = 500$.

development of the stationary crossflow vortex can be captured by a model which considers 0, β and 2β modes.

The interacting case with stationary vortex amplitude 10 times higher than that of the travelling mode is shown in figure 16(*b*). This case is meant to simulate moderately low turbulence conditions where wall roughness will introduce the dominant instability (i.e. a stationary vortex) and the weak turbulence will introduce travelling disturbances with low amplitude. On the other hand, figure 16(*a*) can be thought of as the case with ultra-low turbulence with essentially no travelling modes induced. In contrast, figure 16(*c*) is the high-turbulence case where the initial amplitude of the travelling mode is equal to the stationary mode. Admittedly, these are all idealized cases, for in the natural environment energy input is into a broad band of frequencies and wavenumbers which we cannot attempt to tackle in the present framework.

Figure 16(*b*) shows that the energy in the stationary as well as the travelling modes saturates at about $R = 490$, the energy in the latter mode remains smaller except near the very end at about $R = 600$ where the two become the same. This is also where the energy in mode $(1, -1)$ supersedes the two primary modes and becomes comparable with the mean flow correction mode. The mode $(1, -1)$ is generated from interaction between $(1, 1)$ and $(0, -2)$ mode and, apparently, the combination of the amplitudes is just about right to yield a resonance between the three modes as speculated in §4.1 above.

The situation changes when the initial amplitudes of the two waves become the same. The travelling mode has the higher energy all the way and it tends to suppress the growth of the stationary modes. Both the primary modes saturate earlier, at about $R = 430$ as compared to 490 in figure 16(*b*). The higher modes gaining the dominant energy appear to be $(2,2)$, $(3,3)$, $(4,4)$...modes in this case. The suppression (also compare figures 17*a* and 17*c* below) of the stationary vortices by travelling modes is supported by the observation made in the DLR experiment.

The evolution of the maximum (in y) disturbance amplitude for the three cases is

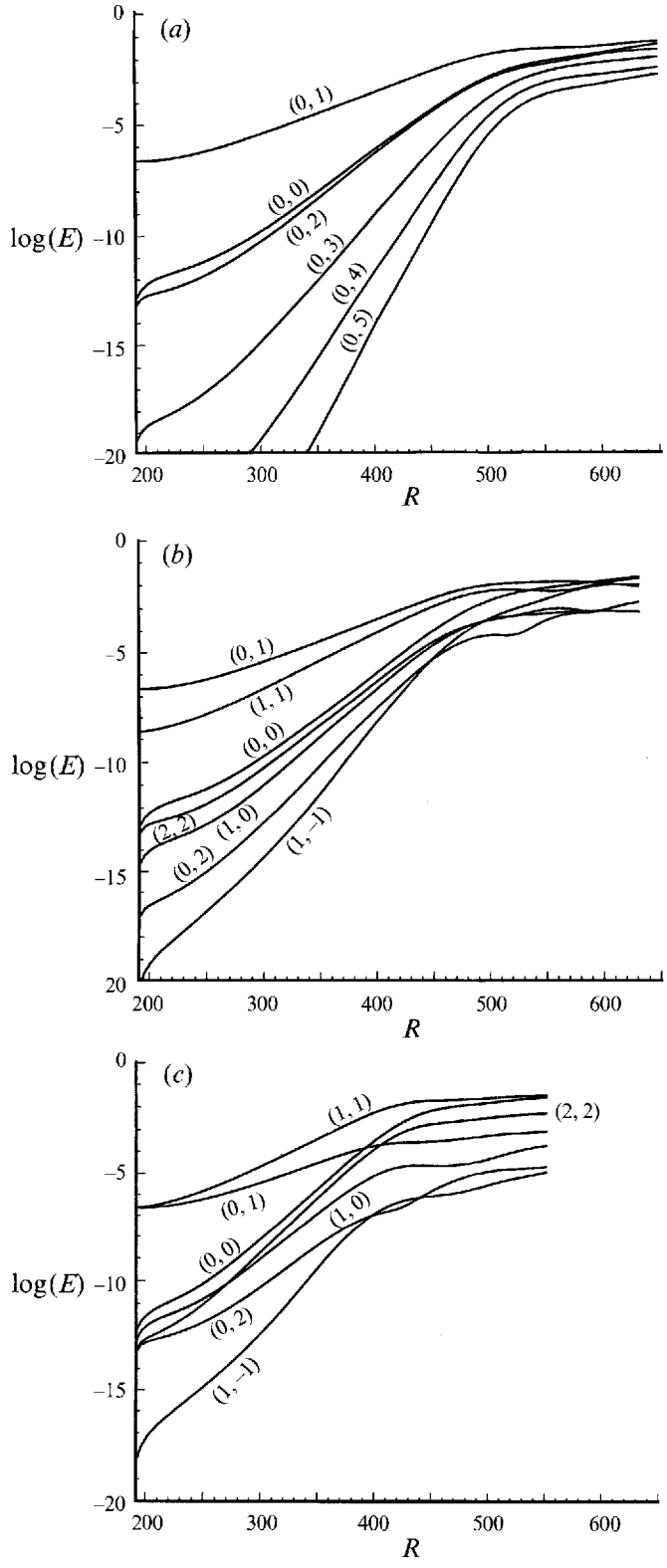

FIGURE 16. For caption see facing page.

given in figure 17 on a natural log scale. Amplitudes of all the velocity components are given. Initially the spanwise velocity $\hat{w}$ is higher than the chordwise velocity $\hat{u}$. Later the magnitudes of the two switch as the inviscid streamline angle decreases (note that $\theta = 45°$ when $R = 500$). The magnitude of the normal velocity $\hat{v}$ is much lower than $\hat{u}$ and $\hat{w}$ for both waves at all R. From figure 17(*a*) for stationary vortices alone, it is clear that the nonlinear N factors ($\ln A/A_0$) at $R = 650$ are 7 and 5 for $\hat{u}$ and $\hat{w}$. These are to be contrasted with the value of about 9 given by quasi-parallel linear calculations in figure 3.

The growth rates of the stationary and travelling waves for the above three cases, along with an additional case of a travelling mode only (initial amplitude of 0.1 %), are given in figure 18. For comparison, the growth rate from linear PSE calculations is also given. This plot more clearly shows the behaviour of the two modes discussed with reference to figure 16. The growth rate of the stationary vortex (curve 2) begins to depart from linear theory at about $R = 420$. At this location the disturbance amplitude is only about 4 %. At $R = 450$, the growth rate is lower than the linear theory result by about 9 %, but it begins to decrease rapidly beyond that. The results are similar for the travelling mode alone (curve 2) with initial amplitude of 0.1 %. Since the travelling mode amplifies more rapidly, it reaches saturation earlier and its growth rate begins to depart from the linear theory results at $R = 330$. For the wave interaction case with $A_t = 0.01$ %, the growth rates of the two waves begin to depart from the linear theory result at about $R = 390$. At $R = 450$ the two growth rates differ from the linear results by about 18 %, subsequently, dropping sharply, and at $R = 500$, the stationary and travelling disturbance growth rates are lower by about 70 and 76 % with respect to their linear growth rates. Hence, the results indicate that even for the case with smaller initial travelling disturbance amplitude there is some interaction well before $R \approx 500$. This interaction becomes stronger when the initial amplitudes of the two waves are the same ($A_s = A_t = 0.1$ %). In this case the growth rates begin to depart from the linear theory results at $R = 330$ and by 410 have dropped by 68 % for the stationary vortex and by 39 % for the travelling mode. A close examination of the results show that when $A_t = 0.1$ %, there is no direct effect of the stationary disturbance on the travelling wave (curves 3 and 5 collapse) but the growth of the stationary vortex is greatly suppressed owing to the presence of higher-amplitude travelling disturbance. It is clear that the two modes do interact depending upon the initial amplitude, as also inferred by Bippes (1991) from his experiments. The nonlinear growth rate behaviour at large R indicates that the two primary modes reach a quasi-equilibrium state where the growth rate begins to oscillate around a small value.

In order to shed some more light on the stationary/travelling mode interaction, we consider the case with $A_s = 0.1$ %, $A_t = 0.01$ %, and plot $\tilde{u}_{rms}$ in the (y, z)-plane at three different Reynolds numbers ($R = 431$, 500 and 600). Here $\tilde{u}_{rms}$ is defined as

$$\tilde{u}_{rms}(x, y, z) = \left[\frac{\omega}{2\pi}\int_0^{2\pi/\omega} u^2(x, y, z, t)\,\mathrm{d}t - u_0^2\right]^{\frac{1}{2}}.$$

The results are shown in figure 19 for the three locations. Owing to nonlinearity and interaction with the stationary mode, travelling disturbances are modulated in the spanwise direction. An important observation is that the peak r.m.s. perturbation is

FIGURE 16. Evolution of integrated (over y) disturbance energy for various modes at $\bar{R} = 500$; the first index refers to frequency and the second index refers to spanwise wavenumber. (*a*) $A_s = 0.1$ %, $A_t = 0$; (*b*) $A_s = 0.1$ %, $A_t = 0.01$ %; (*c*) $A_s = 0.1$ %, $A_t = 0.1$ %. (Subscript s denotes stationary and t travelling.)

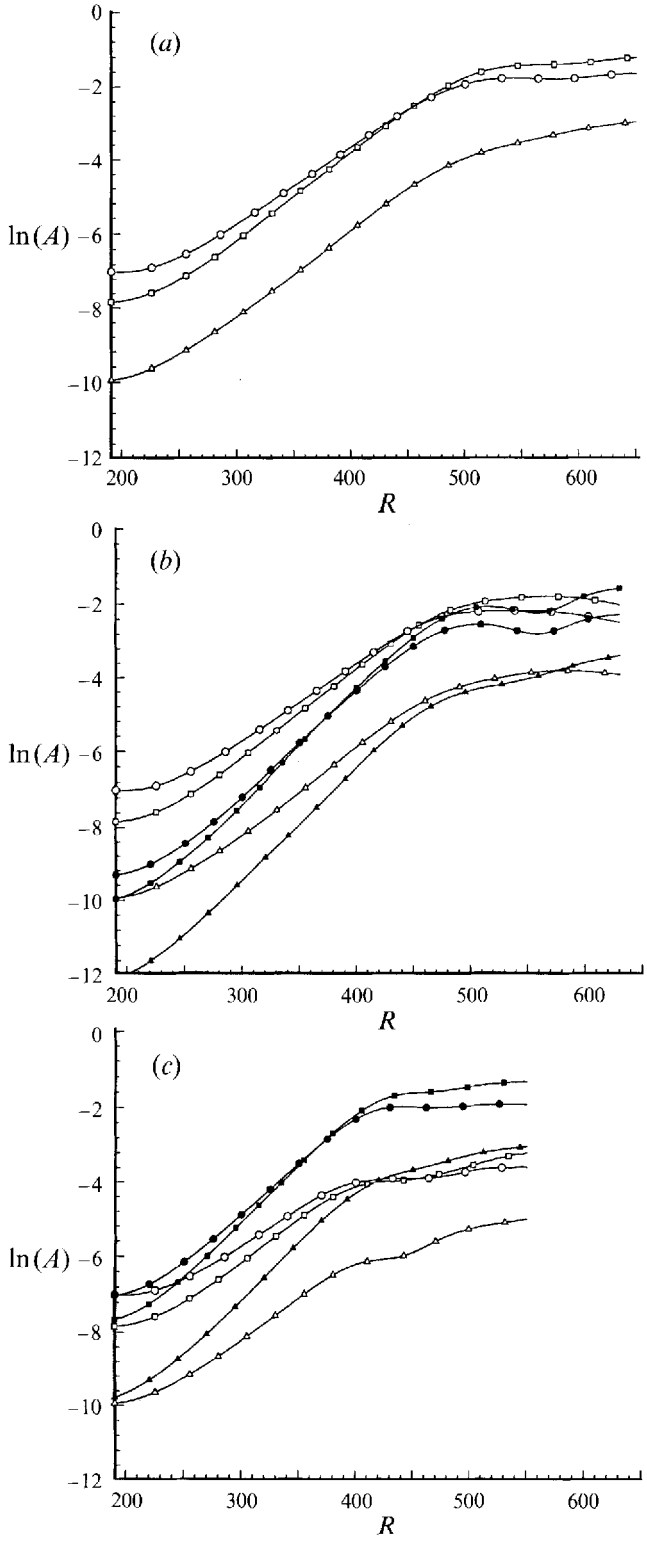

FIGURE 17. For caption see facing page.

near the wall at $y \approx 1$ with a second maximum (but with much lower amplitude) further away from the wall (see figure 19*b*). A comparison of figures 19(*b*) and 10(*b*), at $R = 500$, shows that the peak $\tilde{u}_{rms}$ occurs in the spanwise region where low-velocity fluid is pushed away from the wall. At higher Reynolds number ($R = 600$), there are two peaks in $\tilde{u}_{rms}$ near the wall, apparently associated with the emergence of the 2β harmonic of the stationary mode. Michel, Arnal & Juillen (1985) also noted two maxima in the r.m.s. value of the streamwise velocity within a spanwise wavelength in the ONERA/CERT swept-wing experiment. The magnitude of the maximum value was found to be up to about 20% of the resultant inviscid velocity. They also found that most of the turbulence energy is contained in the frequency range that is unstable according to the linear stability analysis.

Figure 20 is a plot of the stationary as well as r.m.s. velocity signal (*u*-component) at $y = 1.048$. Modulation of the travelling disturbances due to the presence of the stationary vortex is evident. The peak $\tilde{u}_{rms}$ is in the region where a velocity defect appears in the stationary signal and the minimum in $\tilde{u}_{rms}$ occurs where there is a velocity excess. However, there is a phase shift of about $\frac{1}{4}\pi$ between the maximum in $\tilde{u}_{rms}$ and the minimum stationary velocity, as evident from results for $R = 500$. This phase shift decreases at higher Reynolds numbers. Müller & Bippes (1988) reported experimental results qualitatively similar to those in figure 20.

We plot the variation of $\tilde{u}_{rms}$ with Reynolds number at $y = 1.048$ in figure 21, which shows the maximum and minimum $\tilde{u}_{rms}$ as well as $\tilde{u}_{rms}$ along the path where the stationary *u*-velocity has a maximum and a minimum. The variation of the stationary *u*-velocity with Reynolds number is also shown in the figure. Figure 21 clearly shows that in the high (stationary)-velocity region the $\tilde{u}_{rms}$ component gets saturated but it increases to higher amplitudes in the low (stationary)-velocity region. At $R \approx 550$, the maximum $\tilde{u}_{rms}$ reaches about 20% in the low-velocity region. Such high levels, although dependent upon the initial disturbance amplitude, are not unexpected in view of the experimental evidence provided by Michel *et al.* (1985). Poll (1985) also observed a travelling disturbance with frequency close to the most-amplified disturbance given by linear theory. He further noted that close to the surface the amplitude of these disturbances can exceed 20% of the local mean-flow velocity. However, the r.m.s. amplitudes measured by Dagenhart *et al.* (1989) are much lower, which suggests that in their experiment the initial amplitude of travelling modes relative to the stationary mode was much lower than used here. Choudhari (1993) estimates that the initial amplitude of the travelling mode could be up to two orders of magnitude lower than the stationary modes for the receptivity mechanism considered in this study. This may possibly be the case in the experiment of Dagenhart *et al.* (1989).

4.5. *Effect of nonlinear disturbances on skin friction*

Figure 22 gives the chordwise (C_{fu}) and spanwise (C_{fw}) skin-friction coefficients for all three cases. From figure 9 we know that skin friction varies in the spanwise direction. However, figure 22 gives the spanwise-averaged value, i.e. only the contribution from mean flow distortion is considered. Since $\bar{w}$ is independent of R, the laminar spanwise skin friction remains constant. Similarly, since $\bar{u}$ increases linearly with R, so does the chordwise skin friction when scaled with W_∞^2. At some location both C_{fu} and C_{fw} begin to depart from their respective laminar values. For cases (*a*) and (*b*) of figure 16, this location is at about $R = 450$ and from there on it rises significantly. The skin friction

FIGURE 17. Evolution of maximum (over y) amplitude of the disturbance velocity components $\hat{u}$ (—□—), $\hat{v}$ (—△—), $\hat{w}$ (—○—) for stationary (open symbols) and travelling (solid symbols) modes. (*a*) $A_s = 0.1\%$, $A_t = 0$; (*b*) $A_s = 0.1\%$, $A_t = 0.01\%$; (*c*) $A_s = 0.1\%$, $A_t = 0.1\%$.

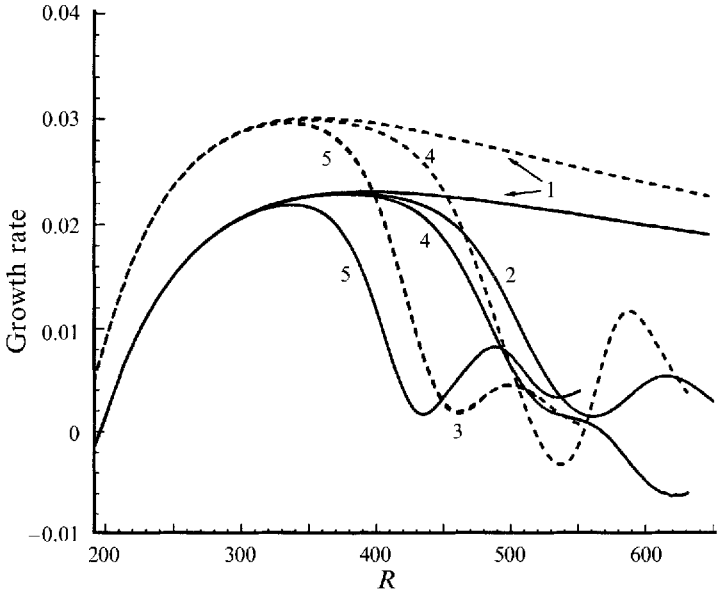

FIGURE 18. Growth rate of stationary (——) and travelling (– – –) modes with and without interaction. Curve 1, linear; 2, $A_s = 0.1\%$, $A_t = 0$; 3, $A_s = 0$, $A_t = 0.1\%$; 4, $A_s = 0.1\%$, $A_t = 0.01\%$; 5, $A_s = 0.1\%$, $A_t = 0.1\%$.

rise from stationary vortex alone is about 19% for C_{fu} and 58% for C_{fw} at $R = 600$. The skin friction for case (*b*) is slightly higher in the beginning but later on it drops below case (*a*). Computations for case (*a*) were made using $N = 2$, 9 and 16 in (3.5). While there was considerable difference in the skin-friction distribution for $N = 2$ and 9, essentially no difference was found between the two higher-resolution cases. For cases (*b*) and (*c*) $M = N = 9$ was used in (3.5).

In case (*c*), with higher initial amplitude of the travelling mode, skin friction begins to rise much earlier at about $R = 375$ as would be expected from the comparison of figure 16(*b*) and 16(*c*) which shows that the mean flow distortion is higher in the latter case. Hence, a stronger interaction of the travelling and stationary modes leads to a higher skin-friction coefficient. Our results indicate that the angle between wall shear and inviscid free stream decreases as the disturbed flow enters the highly nonlinear stage in the three-dimensional boundary layer.

5. High-frequency secondary instability

A hot wire placed in a three-dimensional boundary layer, subject to crossflow instability, sees two types of unsteady disturbances. First, it captures an unsteady signal with a peak at a frequency F_1 which coincides with the most-amplified frequency given by the linear stability theory. In the present case, for example, $F_1 \approx 1.2 \times 10^{-4}$ at $R = 300$ (see figure 5). The dimensional value of this frequency depends upon the flow parameters (unit Reynolds number, sweep, etc.). Poll (1985), for his swept-cylinder experiment, found F_1 to be 1500 Hz for the chord Reynolds number of 1.2×10^6 and sweep angle of 63°. In Kohama *et al.* (1991), F_1 was close to 180 Hz and in Michel *et al.* (1985) $F_1 < 200$. In these experiments, the hot wire also captures a second frequency F_2 which is an order of magnitude larger than F_1. For example, F_2 was 17500, 3500 and 1000 Hz in the experiments of Poll (1985), Kohama *et al.* (1991) and Michel *et al.*

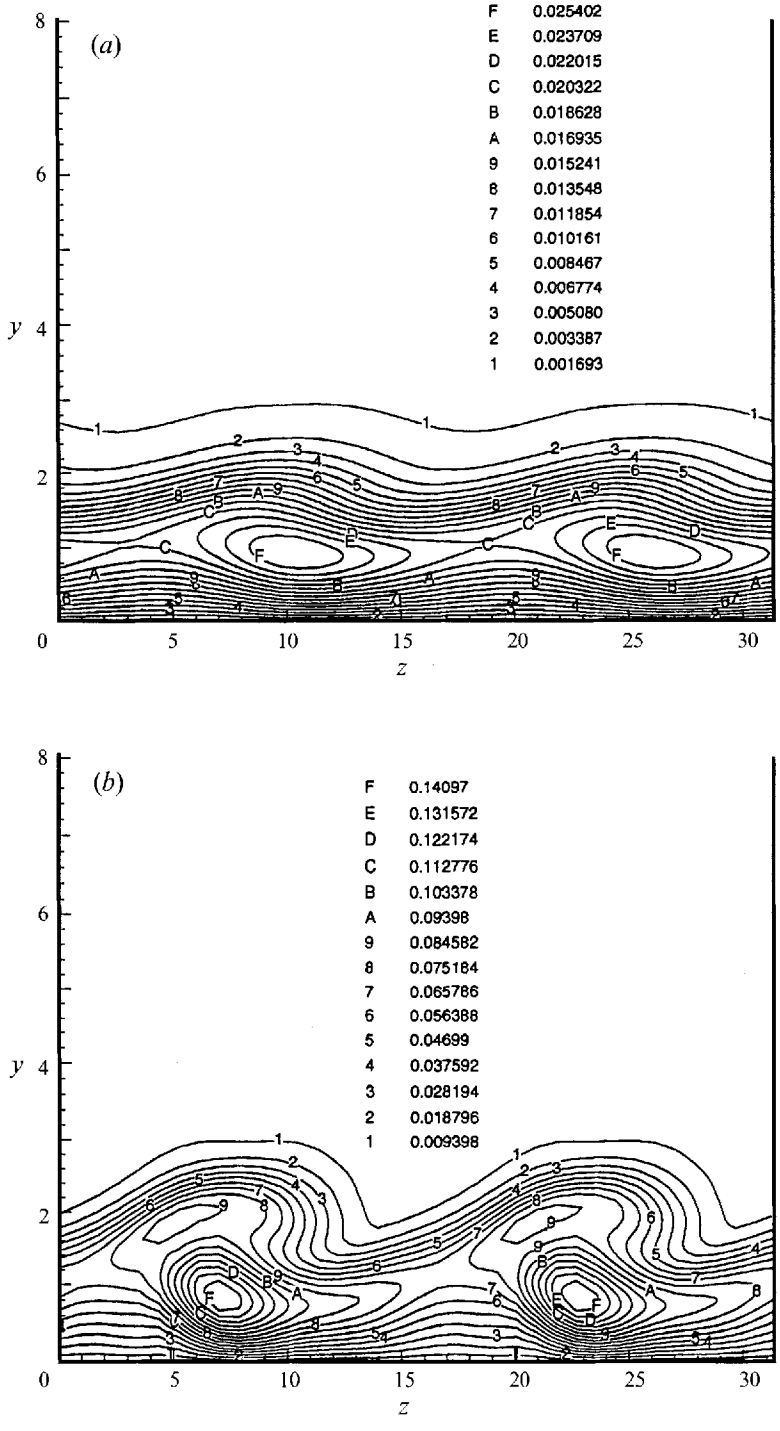

FIGURE 19(*a*, *b*). For caption see facing page.

(1985), respectively. In this section, we investigate this high-frequency instability in the present three-dimensional boundary layer. The problem is modelled here as the secondary instability of the new mean flow that is set up by the presence of a large-amplitude stationary crossflow vortex.

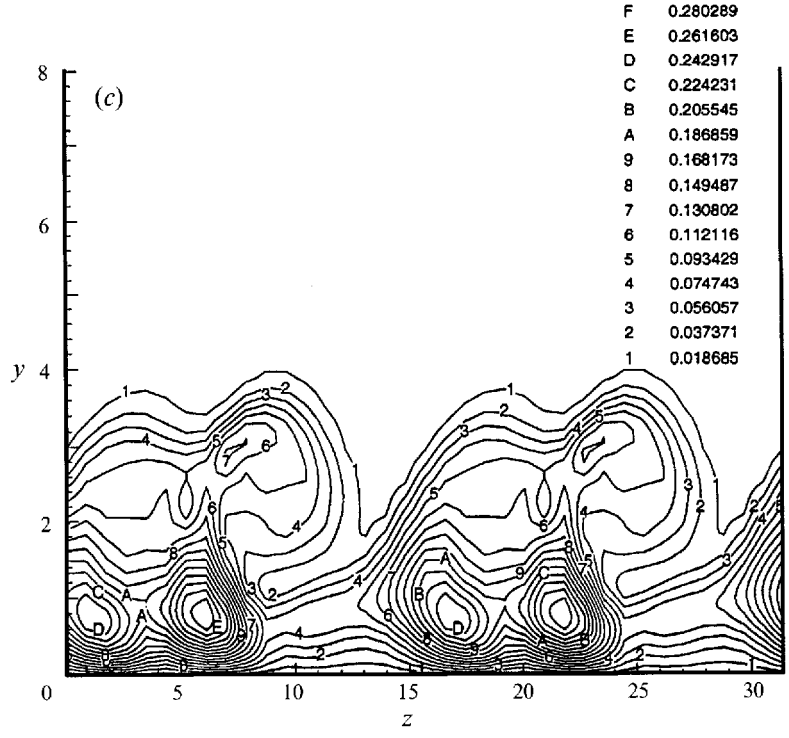

FIGURE 19. Variation of $\tilde{u}_{rms}$ in the (y, z)-plane for the wave interaction case with $A_t = 0.01\,\%$. (*a*) $R = 431$, (*b*) $R = 500$, (*c*) $R = 600$.

We perform a secondary instability analysis locally, i.e. at a fixed Reynolds number and perform a temporal stability analysis. In order to do this analysis, we rotate the (x, z)-coordinates to a new system, x_2, z_2 so that the x_2 coordinate aligns with the crossflow vortex. At a streamwise location designated by the Reynolds number R, we ignore the curvature of the vortex and use the quasi-parallel approximation (we will provide *a posteriori* justification for these assumptions later) which allows us to consider a harmonic disturbance of the type

$$\phi(x_2, y_2, z_2, t) = \phi_2(y_2, z_2, t)\, e^{i(\alpha_2 x_2 - \omega_2 t)}, \tag{5.1}$$

where α_2 and ω_2 are the wavenumber and frequency of the secondary disturbance and $y_2 = y$. Here, since we use the temporal stability concept, α_2 is real and ω_2 is complex. If $\omega_{2i} > 0$ ($\omega_{2i} = \mathrm{Im}(\omega_2)$), then the secondary instability is present. A temporal stability approach has earlier been used by Herbert (1983) for secondary instability of TS waves and by Hall & Horseman (1991) for secondary instability of Görtler vortices. This approach can, at least, provide a qualitative picture of the secondary instability phenomenon.

We superimpose (5.1) on the mean flow computed in §4.3 above, i.e. the mean flow constitutes the three-dimensional boundary layer as modulated by the presence of a nonlinear stationary crossflow vortex with initial amplitude of 0.1 %. This mean flow, when represented in the (x_2, y_2, z_2) coordinate system, is a strong function of y_2 and z_2 but a weak function of x_2. Substituting the mean flow and the disturbance wave (5.1) in the incompressible Navier–Stokes equations, we obtain the following linearized equations:

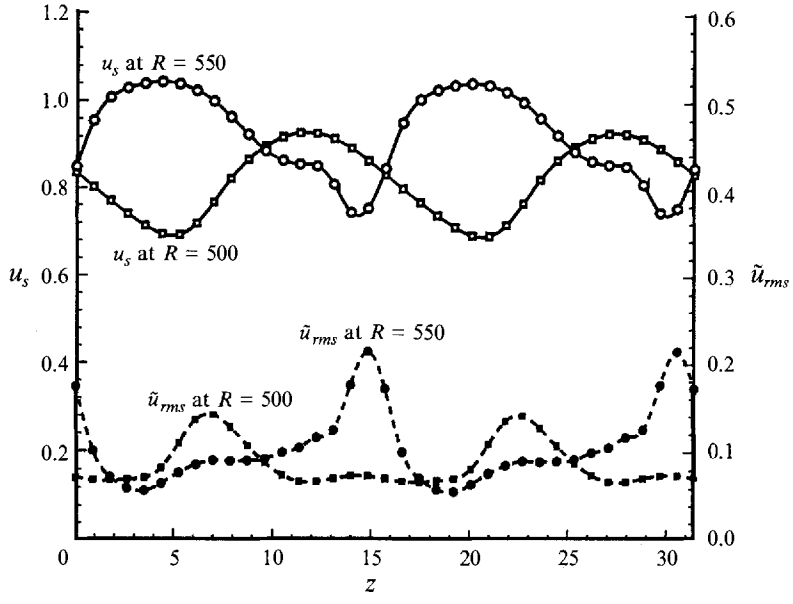

FIGURE 20. Spanwise variation of chordwise velocity (u_s and $\tilde{u}_{rms}$) at $y = 1.048$ for the wave interaction case with $A_t = 0.01\,\%$.

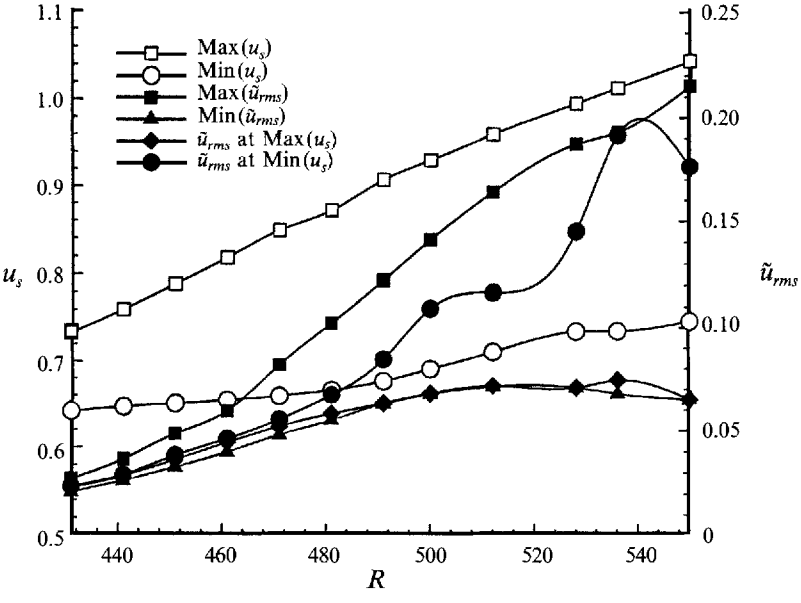

FIGURE 21. Variation of maximum and minimum u_s and $\tilde{u}_{rms}$ at $y = 1.048$ with Reynolds number. $\tilde{u}_{rms}$ at locations where u_s is maximum and minimum is also given.

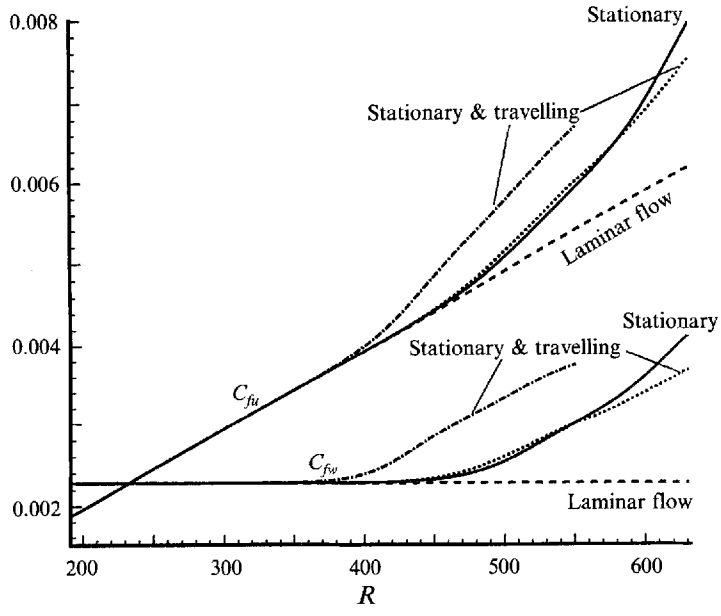

FIGURE 22. Chordwise (C_{fu}) and spanwise (C_{fw}) skin-friction coefficients for cases (*a*), (*b*), (*c*) of figure 16.

$$\left[\mathrm{i}\alpha_2 U_2+\frac{\alpha_2^2}{R}+\frac{\partial U_2}{\partial x_2}\right]u_2+\frac{\partial U_2}{\partial y_2}v_2+\frac{\partial U_2}{\partial z_2}w_2+\mathrm{i}\alpha_2 p_2+V_2\frac{\partial u_2}{\partial y_2}+W_2\frac{\partial u_2}{\partial z_2}-\frac{1}{R}\left[\frac{\partial^2 u_2}{\partial y_2^2}+\frac{\partial^2 u_2}{\partial z_2^2}\right]=\mathrm{i}\omega_2 u_2, \tag{5.2}$$

$$\frac{\partial V_2}{\partial x_2}u_2+\left[\mathrm{i}\alpha_2 U_2+\frac{\alpha_2^2}{R}+\frac{\partial V_2}{\partial y_2}\right]v_2+\frac{\partial V_2}{\partial z_2}w_2+V_2\frac{\partial v_2}{\partial y_2}+W_2\frac{\partial v_2}{\partial z_2}+\frac{\partial p_2}{\partial y_2}-\frac{1}{R}\left[\frac{\partial^2 v_2}{\partial y_2^2}+\frac{\partial^2 v_2}{\partial z_2^2}\right]=\mathrm{i}\omega_2 v_2, \tag{5.3}$$

$$\frac{\partial W_2}{\partial x_2}u_2+\frac{\partial W_2}{\partial y_2}v_2+\left[\mathrm{i}\alpha_2 U_2+\frac{\alpha_2^2}{R}+\frac{\partial W_2}{\partial z_2}\right]\omega_2+V_2\frac{\partial w_2}{\partial y_2}+W_2\frac{\partial w_2}{\partial z_2}+\frac{\partial p_2}{\partial z_2}-\frac{1}{R}\left[\frac{\partial^2 w_2}{\partial y_2^2}+\frac{\partial^2 w_2}{\partial z_2^2}\right]=\mathrm{i}\omega_2 w_2, \tag{5.4}$$

$$\mathrm{i}\alpha_2 u_2+\frac{\partial v_2}{\partial y_2}+\frac{\partial w_2}{\partial z_2}=0, \tag{5.5}$$

where U_2, V_2, W_2 are the mean velocity components in the x_2-, y_2-, z_2-directions, respectively, u_2, v_2, w_2 are the corresponding disturbance velocity components and p_2 is the pressure. In (5.2)–(5.4) $\partial U_2/\partial x_2$, $\partial V_2/\partial x_2$, $\partial W_2/\partial x_2$ are small and can be neglected as numerical experiments indicate that they do not appreciably change the eigenvalue. However, $\partial V_2/\partial y_2$ is of the same order as $\partial W_2/\partial z_2$ and thus V_2 must not be set to zero. Dropping V_2 increases the growth rate by about 50%. Equations (5.2)–(5.5) are partial differential equations which are subject to homogeneous conditions at the wall and free stream, i.e.

$$u_2=v_2=w_2=0, \quad y_2=0, \tag{5.6a}$$

$$u_2\to 0, \quad v_2\to 0, \quad w_2\to 0 \quad \text{as} \quad y_2\to\infty. \tag{5.6b}$$

The computational domain in the z_2-direction covers one wavelength of the stationary vortex and periodic boundary conditions are imposed in the z_2-direction, i.e.

$$u_2(z_2) = u_2(z_2 + \lambda_z), \tag{5.7a}$$

$$v_2(z_2) = v_2(z_2 + \lambda_z), \tag{5.7b}$$

$$w_2(z_2) = w_2(z_2 + \lambda_z), \tag{5.7c}$$

where $\lambda_z = 2\pi/(\alpha_s^2 + \beta_s^2)^{\frac{1}{2}}$, α_s and β_s being the x and z wavenumbers of the stationary vortex.

Equations (5.2)–(5.5) along with the boundary conditions (5.6)–(5.7) constitute an eigenvalue problem which we solve by using a Chebyshev collocation method in the y_2-direction and a Fourier collocation method in the z_2-direction. The physical domain $y_2 \in [0, y_{2_{max}}]$ is mapped on to a computational domain $\eta \in [-1, 1]$ such that the grid points are clustered near the wall and $y_2 = y_{2_i}$, where y_{2_i} is the location where the secondary structure is concentrated. Since we do not stagger the mesh in the y_2-direction, two additional boundary conditions are required, which we prescribe by evaluating the normal momentum equation at $y_2 = 0$ and $y_{2_{max}}$.

The eigenvalue problem can be represented in the form

$$\boldsymbol{A}\boldsymbol{\varphi} = \omega_2 \boldsymbol{B}\boldsymbol{\varphi} \tag{5.8}$$

where $\boldsymbol{B}$ is a diagonal matrix and $\boldsymbol{A}$ is a square matrix of size $(4N_y - 6)N_z$ where N_y and N_z are the number of collocation points in the y_2- and z_2-directions, respectively. The eigenvalue problem (5.8) is solved by the QR method which yields all the eigenvalues of the discretized system. We test the accuracy of these eigenvalues by using the inverse Rayleigh iteration method. Among the computed eigenvalues, only a few have $\omega_{2_i} > 0$. Here, we discuss only one of these eigenvalues.

Computations were first performed at $R = 450$ where the stationary crossflow disturbances had gained an amplitude of about 8% based upon the local inviscid velocity (see figure 17*a*). No secondary instability was found, i.e. all $\omega_{2_i} < 0$. The analysis was then repeated at $R = 500$ where the maximum $\hat{u}$-amplitude is about 17% and the stationary vortex is on its way to saturation (compare with figure 18). At this location the secondary instability is found but the growth rate is about the same as that of the nonlinear crossflow vortex. Finally, calculations were performed at $R = 550$, where figure 18 shows that the stationary vortex has a growth rate which is close to zero. The local maximum amplitude of the stationary vortex is about 22%. Secondary instability results for this Reynolds number are discussed next.

The frequency (ω_{2r}) of the secondary instability and temporal growth rate (ω_{2i}) are plotted in figure 23. The peak growth rate of $\omega_{2i} \approx 0.02$ occurs at α_2 of about 0.6. At this location ω_{2r} is about 0.75 which amounts to an F_2 of 1.5×10^{-3}. We noted earlier that the most-amplified travelling crossflow disturbance has a frequency of about $F_1 \approx 1.2 \times 10^{-4}$; hence, F_2 is an order of magnitude higher than F_1, which is in agreement with the experiments mentioned above. The wavenumber of the stationary disturbance along the z_2-coordinate is about 0.5. Given that α_2 is 0.6, the angle of the secondary structure is about 50° with respect to the crossflow vortex. The secondary instability convects along the stationary vortex with the phase velocity of about 1.25 W_∞. The relatively high amplitude of the stationary vortex required for secondary instability is in agreement with the results of Balachandar *et al.* (1992).

The above calculations were made with $N_y = 41$ and $N_z = 8$. Since 8 collocation points in the spanwise direction may be too few, we repeated some of the calculations with $N_z = 16$ and $N_y = 51$. These results are also given in figure 23. We note that

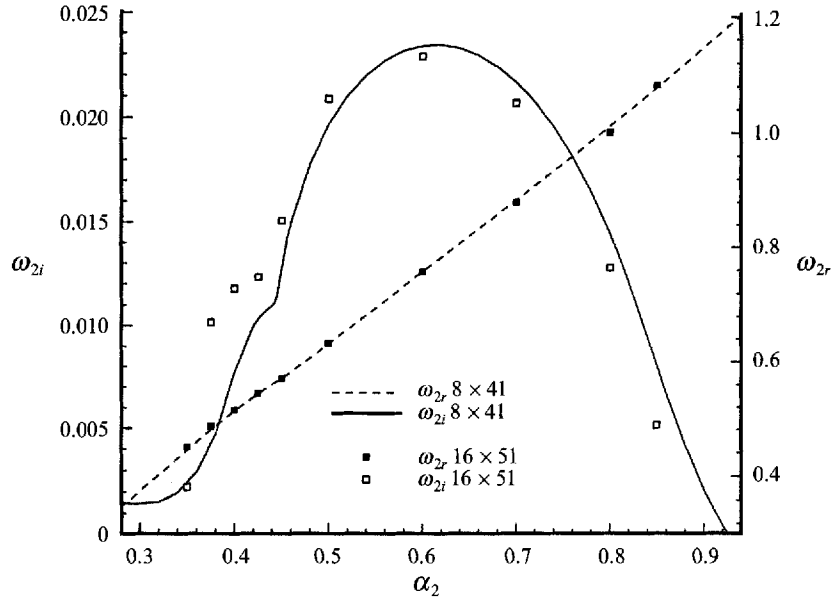

FIGURE 23. Temporal growth rate and frequency of the secondary instability in the three-dimensional boundary layer at $R = 550$. Results for two different numerical resolutions are shown.

although there is some movement in the eigenvalues, the results with the lower resolution are qualitatively correct, at least at high α_2. At lower values of the wavenumber α_2, there appears to be an intricate mode structure, the investigation of which would require the development of more efficient means of computing eigenvalues of very large matrices.

The quasi-parallel approximation used in the above analysis can be justified since our results show that, in the rotated coordinate system, variations of U_2, V_2, W_2 along x_2 are much smaller than the variations in y_2, z_2, and the x_2-wavelength of the secondary instability is only about three times the boundary-layer thickness. In the non-dimensional units, this wavelength for the most-amplified secondary wave is about 10. The secondary instability analysis shown in figure 23 is performed at $R = 550$. It is clear from figure 9 that the curvature of the vortex in the range of $R = 550 \pm 5$ can be ignored.

The structure of the secondary instability is presented in figure 24 where the $|u_2|$ eigenfunction is plotted along with the U_2-component of the meanflow in the (y_2, z_2)-plane at $R = 550$. It is clear that this high-frequency instability resides on top of the stationary vortex with the maximum in $|u_2|$ located near $y_2 \approx 2.8$. In contrast, the lower-frequency travelling crossflow disturbance is concentrated near the wall at $y_2 \approx 1$ (see figure 19). The high-frequency instability is inviscid in nature and it can be captured by dropping viscous terms in (5.2)–(5.4); however, since the basic flow is three-dimensional and varies with y_2 and z_2 it is not possible to reduce the problem to a single partial differential equation. However, numerical experiments suggest that some qualitative features of the instability can be captured by considering just the U_2-component of the mean flow in which case a single partial differential equation can be used resulting in substantial savings in computer time.

The top view of the flow field that results by superimposing the secondary eigenstructure (with an amplitude of 5%) on the mean flow (U_2, V_2, W_2) is depicted in figure 25 where the x_2-velocity component is plotted at $y_2 = 2.82$. Two periods in both

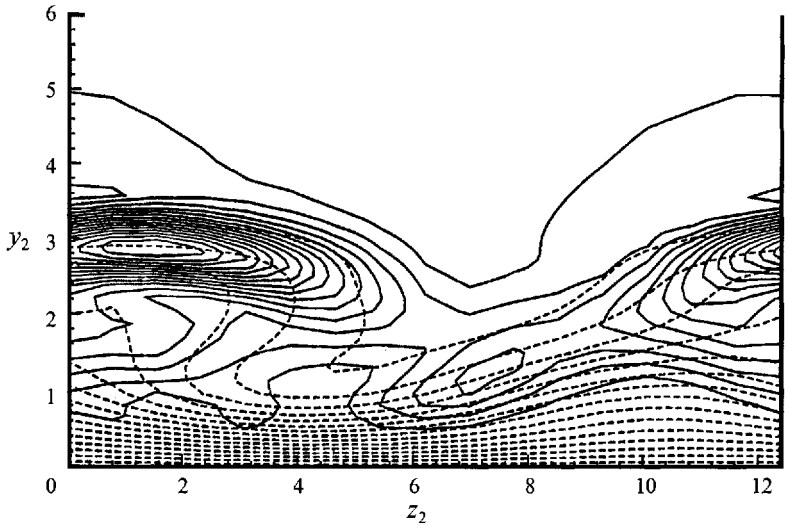

FIGURE 24. The x_2-component of mean flow (dashed lines) and the $|u_2|$ eigenfunction (solid lines).

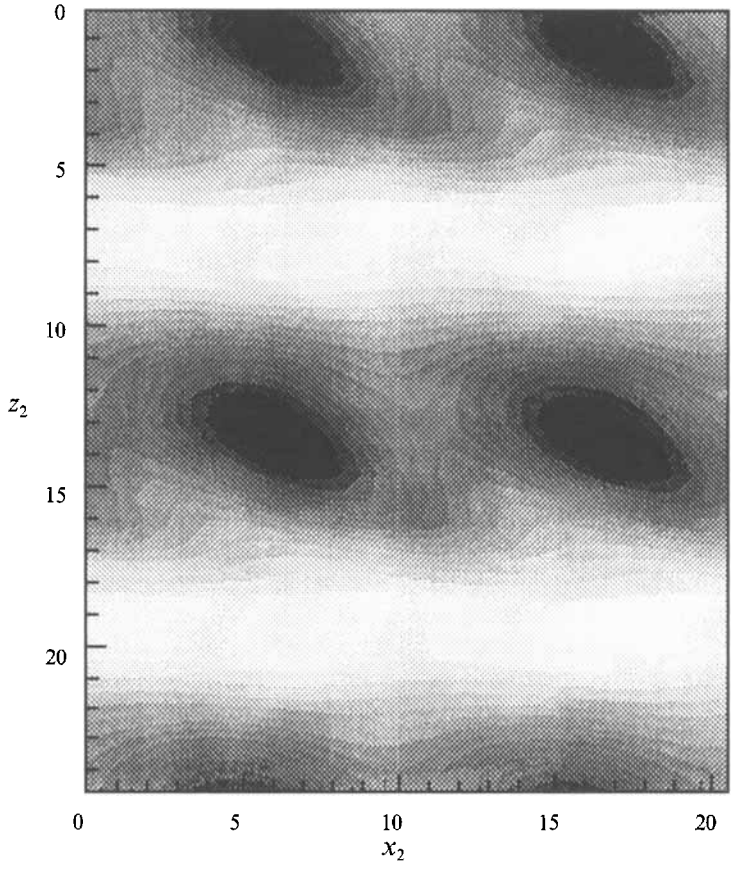

FIGURE 25. The distribution of the x_2-total velocity component in the (x_2, z_2)-plane at $y_2 = 2.82$. The $|u_2|$ eigenfunction was assigned an amplitude of 5%.

the x_2- and z_2-directions are shown. The dark patches in the picture correspond to the corotating structures which move in the x_2-direction. A hot wire placed near the boundary-layer edge will detect this high-frequency disturbance but if the hot wire is located in the region between $z_2 = 5$ and 10, for example, this instability will not be captured. Therefore, extreme care is needed in order to detect this secondary structure in an experiment.

6. Conclusions

We have investigated crossflow instability in a model three-dimensional boundary layer which has an exact solution to the incompressible Navier–Stokes equations. This consists of the swept-Hiemenz flow which forms near an attachment line. This flow is subject to Tollmien–Schlichting instability for small x, where x is the chordwise distance, provided the spanwise Reynolds number $\bar{R} > 583.1$. However, this boundary layer becomes unstable to crossflow instability for $x \gg 1$ even for $\bar{R} < 583.1$ Here, we have considered $\bar{R} = 250$ and 500 for the linear stability and $\bar{R} = 500$ for the nonlinear case. Both the linear and nonlinear stability as well as the wave interaction in this three-dimensional boundary layer are studied using parabolized stability equations (PSE). We also study secondary instability in this boundary layer. We find that the various features of the swept-wing boundary-layer transition are captured in the study of this model boundary layer.

Our linear results show that non-parallel effects are destabilizing for crossflow disturbances. However, the magnitude of the effect depends upon $\bar{R}$ (more destabilization at lower $\bar{R}$). Growth rates of stationary crossflow vortices computed from linear PSEs are in agreement with the results obtained from a Navier–Stokes simulation.

Nonlinear development of a stationary crossflow vortex is also investigated for an initial amplitude of 0.1 %. The computed wall vorticity distribution shows the familiar streamwise streaks, in agreement with the surface oil-flow visualizations in swept-wing experiments. Other features of the stationary vortex development observed in the experiments (half-mushroom structure, highly inflected velocity profiles, vortex doubling, etc.) are also captured in our nonlinear PSE computations.

Nonlinear interaction of stationary and travelling crossflow modes is also studied. When the initial amplitude of stationary vortex is large compared to the travelling mode, the stationary vortex dominates most of the downstream development. Eventually, however, the travelling mode becomes of the same order as the stationary mode. Interaction of the travelling mode with the harmonic of the stationary mode gives rise to another travelling mode with same frequency but negative spanwise wavenumber. Apparently, a triad resonance is set up at this stage. The situation changes when the initial amplitudes of the travelling and stationary modes are the same. Owing to its higher growth rate, the travelling mode dominates most of the downstream development and the growth of the stationary mode is suppressed. In this case, energy cascades into (2, 2), (3, 3) etc., modes which are harmonics of the primary (1, 1) travelling mode.

Growth rates of the stationary and travelling modes begin to depart from their linear values when the disturbance amplitude reaches about 4 %. As the amplitude increases, the primary modes reach quasi-equilibrium states. Large mean flow distortion caused by the nonlinear disturbances yields a skin-friction value which is significantly above the laminar value.

Finally, we use the two-dimensional eigenvalue approach to perform a secondary

instability analysis of the three-dimensional boundary-layer flow modulated by the presence of a nonlinear stationary crossflow vortex. We find that this mean flow is subject to an instability whose frequency is an order of magnitude higher than the frequency of the most-amplified travelling mode given by linear stability analysis of the boundary-layer profiles. A similar high-frequency disturbance was also observed in the experiments of Poll (1985) and Kohama *et al.* (1991).

This work was sponsored under AFOSR Contract F49620-91-C-0014. Computer time was provided by NASA Langley Research Center. The authors thank their colleague R.-S. Lin, for his assistance in this work. The authors would like to express their gratitude towards Dr Craig Streett at NASA Langley for providing his as yet unpublished data from Navier–Stokes calculations.

REFERENCES

ARNAL, D. & JUILLEN, J. C. 1987 *AIAA Paper* 87-1335.

BALACHANDAR, S., STREETT, C. L. & MALIK, M. R. 1992 *J. Fluid Mech.* **242**, 323.

BERTOLOTTI, F. P., HERBERT, TH. & SPALART, P. R. 1992 *J. Fluid Mech.* **242**, 441.

BIPPES, H. 1991 In *R. Aeronaut. Soc. Conf. on Boundary Layer Transition & Control, Cambridge, UK.*

CHANG, C.-L., MALIK, M. R., ERLEBACHER, G. & HUSSAINI, M. Y. 1991 *AIAA Paper* 91-1636.

CHOUDHARI, M. M. 1993 *Theor. Comput. Fluid Dyn.* **5**, 487.

CHOUDHARI, M. M. & STREETT, C. 1990 *AIAA Paper* 90-5258.

DAGENHART, J. R., SARIC, W. S., MOUSSEUX, M. C. & STACK, J. P. 1989 *AIAA Paper* 89-1892.

FISCHER, T. M. & DALLMANN, U. 1991 *Phys. Fluids* A **3**, 2378.

GRAY, W. E. 1952 *R. Aeronaut. Establ. Tech. Memo.* (*Aero*) 256.

GREGORY, N., STUART, J. T. & WALKER, W. S. 1955 *Phil. Trans. R. Soc. Lond.* A **248**, 155.

HALL, P. & HORSEMAN, N. J. 1991 *J. Fluid Mech.* **232**, 357.

HALL, P., MALIK, M. R. & POLL, D. I. A. 1984 *Proc. R. Soc. Lond.* A **395**, 229.

HERBERT, TH. 1983 *Phys. Fluids* **26**, 871.

HERBERT, TH. 1991 *AIAA Paper* 91-0737.

JOSLIN, R. D., STREETT, C. L. & CHANG, C.-L. 1992 *NASA TP*-3205.

KOHAMA, Y. 1984 *Acta Mechanica* **50**, 193.

KOHAMA, Y. 1987 *AIAA Paper* 87-1340.

KOHAMA, Y., SARIC, W. S. & HOOS, J. A. 1991 In *Proc. R. Aeronaut. Soc. Conf. on Boundary Layer Transition & Control, Cambridge, UK*, p. 4.1.

MACK, L. M. 1985 *AIAA Paper* 85-0490.

MALIK, M. R. 1986 In *10th Intl Conf. on Numerical Methods in Fluid Dynamics* (ed. F. G. Zhuang & Y. L. Zhu), p. 455. Springer.

MALIK, M. R., CHUANG, S. & HUSSAINI, M. Y. 1982 *Z. Angew. Math. Phys.* **33**, 189.

MALIK, M. R. & LI, F. 1992 *SAE Paper* 921991.

MALIK, M. R. & LI, F. 1993 *AIAA Paper* 93-0077.

MEYER, F. & KLEISER, L. 1988 In *AGARD Conf. Proc.* 438, p. 16-1.

MICHEL, J. M., ARNAL, D. & JUILLEN, J. C. 1985 In *Laminar Turbulent Transition* (ed. V. V. Kozlov), p. 553. Springer.

MÜLLER, B. 1989 *Laminar-Turbulent Transition* (ed. D. Arnal & R. Michel), p. 489. Springer.

MÜLLER, B. & BIPPES, H. 1988 In *AGARD Conf. Proc.* 438, p. 13-1.

PEERHOSSAINI, H. & WESFREID, J. E. 1988 *Intl J. Heat Fluid Flow* **9**, 12.

POLL, D. I. A. 1985 *J. Fluid Mech.* **150**, 329.

REED, H. L. 1987 *Phys. Fluids* **30**, 3419.

SARIC, W. S., DAGENHART, J. R. & MOUSSEUX, M. C. 1989 In *Numerical and Physical Aspects of Aerodynamic Flows* **4** (ed. T. Cebeci). Springer.

SPALART, P. R. 1988 In *AGARD Conf. Proc.* 438, p. 5-1.

SPALART, P. R. 1989 In *Laminar-Turbulent Transition* (ed. D. Arnal & R. Michel), p. 622. Springer.

SWEARINGEN, J. D. & BLACKWELDER, R. F. 1987 *J. Fluid Mech.* **182**, 255.

WILSON, S. D. R. & GLADWELL, I. 1978 *J. Fluid Mech.* **84**, 517.